

# Coherent time-dependent oscillations and temporal correlations in triangular triple quantum dots

Samuel L. Rudge

*Institute of Physics, Albert-Ludwigs University Freiburg, Freiburg, 79100, Germany*

Daniel S. Kosov

*College of Science and Engineering, James Cook University, Townsville, QLD, 4814, Australia*

The fluctuation behavior of triple quantum dots has, so far, largely focused on current cumulants in the long-time limit via full counting statistics. Given that triple quantum dots are non-trivial open quantum systems with many interesting features, such as Kondo-enhanced scattering, Aharonov-Bohm interference, and coherent population blocking, new fluctuating-time statistics, such as the waiting time distribution (WTD), may provide more information than just the current cumulants alone. In this paper, consequently, we use a Born-Markov master equation to calculate the standard and higher-order WTDs for coherently-coupled triple quantum dots arrayed in triangular ring geometries for several transport regimes. In all cases we find that the WTD displays coherent oscillations that correspond directly to individual time-dependent dot occupation probabilities, a result also reported recently in Ref.[1]. Our analysis, however, goes beyond the single-occupancy and single waiting time regimes, investigating waiting time behavior for triple quantum dots occupied by multiple electrons and with finite electron-electron interactions. We also demonstrate that in these regimes of higher occupancy, quantum coherent effects introduce correlations between successive waiting times, which we characterize both with an averaged approach via the Pearson correlation coefficient, and a quantity  $W(\tau_1, \tau_2)$  that describes correlations between each pair of successive waiting times  $\tau_1$  and  $\tau_2$ .

## I. INTRODUCTION

Due to their small size, great chemical variability, fast transistor signals, and advanced assembly, molecular-sized devices offer the potential to supersede contemporary silicon electronic components [2–4]. These advantages are inherent to nanoscale electronic junction design, in which a nanostructure, such as a molecule or atomic bridge, is chemically bonded to macroscopic metal electrodes. Beyond just technological advantages, furthermore, nanoscale electronic junctions are excellent systems for investigating nonequilibrium quantum physics and are host to many novel phenomena, such as cotunneling [5], vibrationally coupled transport [6, 7], and Kondo-enhanced conductance [8].

Triple quantum dots (TQDs) are a class of molecular junctions with particularly interesting and complex features, which we will explore in this paper. Singular quantum dots are often referred to as “artificial atoms” due to their discrete energy spectrum; so coherently coupling multiple dots together produces an analogous “artificial molecule”: the motivation for producing nanostructures like TQDs. Experimentally, TQDs are usually formed by placing a 2-dimensional electron gas (2DEG) below the surface of a heterostructure, such as GaAs/AlGaAs, depositing metal gates arrayed in an appropriate geometry, and then depleting electrons below the surface via a negative voltage [9–12]. This process is not an easy task, however, and, while singular quantum dot synthesis has been viable for decades, it is only in the last 15 years that experimental techniques have become sophisticated enough to create coherently-coupled doubly [13] and triply [9–12] coupled systems.

The early experiments from Ref.[9–12] focused on TQDs arranged in a triangular ring geometry, which are also the configurations we use throughout the paper and are displayed schematically in Fig.(1a) and Fig.(1b). Other groups have created TQDs in other configurations, such as chain formations [14], star-like formations [15], and parallel-coupled mesa formations [16, 17]. Beyond just experimental realization, however, TQDs offer great potential to fields like quantum computing. Qubits formed from the spin of an electron in a singular quantum dot are vulnerable to decoherence due to magnetic noise from, for example, spins of surrounding nuclei. Qubits defined from the singlet,  $\frac{1}{\sqrt{2}}(|\uparrow\downarrow\rangle - |\downarrow\uparrow\rangle)$ , and triplet,  $\frac{1}{\sqrt{2}}(|\uparrow\downarrow\rangle + |\downarrow\uparrow\rangle)$ , states of two electrons in a DQD, on the other hand, do not lose coherence due to magnetic noise [18]. To go one step further, encoding information in three electrons on a TQD, creating a 3-spin qubit, provides decoherence protection and also greater electrical control [19, 20]. Laird et al., for example, were able to create, measure, and control a 3-spin qubit in a serial TQD system [21]. Gaudrea’s group [22] were later able to provide more control over this system, maintaining coherence while controlling inter-dot spin-coupling strengths. Long-range spin transfer between the two outermost dots in a serial TQD has also been demonstrated [23]. Łuczack and Bułka, meanwhile, have presented theory detailing the coherent manipulation of a 3-spin qubit in a triangular TQD [24, 25].

These last theoretical results are symptomatic of TQD research; since coherent multi-dot synthesis is a relatively new development, the accompanying theory has in many cases far outstripped experiment. Due to the multiple ge-

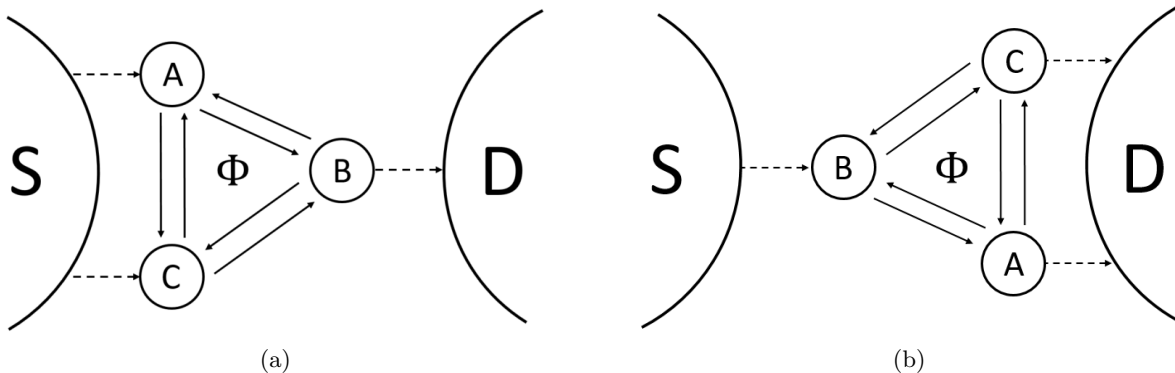


FIG. 1: Schematics of the two triangular TQD geometries used in this chapter. In (a) dots  $A$  and  $C$  are coupled to the source, while dot  $B$  alone is coupled to the drain, and (b) contains the opposite configuration, obtained by rotating the TQD  $180^\circ$  clockwise and coupling dots  $A$  and  $C$  to the drain and dot  $B$  to the source.

ometries, large number of tunable parameters, and complex Fock space, TQDs admit a wide variety of novel phenomena, such as quantum phase transitions [26], charge frustration [27], and spin-entangled current [28]. One of the most interesting and well-explored such effects in the rich TQD literature is the appearance of Kondo physics, which was initially explored for serially coupled configurations [29, 30]. There has also been much interest in the Kondo regime for triangular TQDs [31, 32], where the inter-dot coupling symmetry becomes important [33–35] and Aharonov-Bohm interference affects the formation of the spin-singlet state [36].

Beyond affecting the Kondo physics, Aharonov-Bohm interference actually plays an important role in triangular TQDs when a magnetic flux,  $\Phi$ , is applied perpendicular to the ring interior, as in Fig.(1a) and Fig.(1b). For triangular TQDs, the Aharonov-Bohm effect is often analyzed in conjunction with coherent population trapping. This occurs when the coupling parameters of the TQD are tuned so as to form a “dark” state [37, 38]: a coherent superposition of dot states that block the current. In the configuration depicted in Fig.(1a), and when the occupancy of the three dots is limited to one electron, Emary [39] demonstrated that there exists certain parameters for which  $|\psi_{\text{dark}}\rangle = a|A\rangle + c|C\rangle$  is an eigenstate of the Hamiltonian, decoupling the  $B$  dot, and thus the drain. He also showed that a magnetic flux lifts this coherent blockade and produces Aharonov-Bohm oscillations in the stationary current, and that, at the peak of destructive interference, the Fano factor is super-Poissonian, possibly due to avalanche tunneling.

The dark state is not just a feature of the single electron regime; Poltl et al. [40, 41] and Busl et al. [42] have shown that for double-occupancy of the TQD, with each dot now modeled as an Anderson impurity, spin effects could produce coherent electron trapping if the inter-dot coupling  $U_{\nu\nu'}$  equaled the intra-dot coupling  $U_{\nu\nu}$ . Dark states are evidently an interesting quantum phenomenon, but they can also produce current rectification and negative differential resistance [43]: two promising technolog-

ical applications. If not penetrated by a magnetic flux, a strong molecule-electrode coupling can lift the coherent blockade, as Weymann et al. [44] showed by including cotunneling processes in a triangular TQD, although Noiri et al. [45] has found that cotunneling can introduce an additional spin blockade in serially coupled TQDs. Coherent population trapping also occurs for higher occupancies [46]; for example, under triple-occupancy a coherent spin blockade forms for certain parameters under an applied electric field [47].

There are clearly interesting current fluctuations in a triangular TQD, which have so far been investigated mainly via the current cumulants in the long-time limit. We propose to use fluctuating-time statistics, like the waiting time distribution (WTD) [48] and its cumulants, to analyze coherent charge transport through triangular TQDs in a variety of regimes, and in particular those systems considered by Emary [39] and Poltl et al. [40, 41] for correlations arising from quantum interference in the dark state and moderated by the Aharonov-Bohm effect. WTDs are a relatively recent addition to the fluctuation statistics toolbox and have consistently proven to contain complementary information not available from the long-time FCS alone [49–61]; their ability to describe short-time behavior is particularly relevant when correlations exist between successive waiting times. Previous work on WTDs for TQDs has not investigated correlations [62]; however, within only the last two years Engelhardt and Cao [1] have shown that the WTD for a similar TQD configuration displays oscillatory behavior, which is correlated with relevant occupations of the three dots. We find similar results for the geometries in Fig.(1a) and Fig.(1b), albeit for more complicated transport regimes.

In Section II, we first briefly outline the general Born-Markov master equation (BMME) and the superoperator form necessary to calculate all fluctuation statistics. We then discuss in depth all TQD models and transport regimes used in our analysis in Section III. Section IV, meanwhile, introduces the FCS and WTD, as well as a discussion on renewal and non-renewal behavior. We

present results for all three transport scenarios in Section V well as an explanation for each, with the conclusions contained in Section VI. Relevant derivations are displayed in Appendix A and B.

Throughout the paper we use natural units:  $\hbar = e = k_B = 1$ .

## II. THEORY

Although we exclusively investigate the electrode-TQD-electrode configurations displayed in Fig.(1a) and Fig.(1b), these two schematics are specific examples of the general design paradigm in molecular electronics: a nanostructure coupled to source and drain metal electrodes. In such electrode-nanostructure-electrode devices, the fluctuation statistics naturally originate from the difference between the number of electrons transferred forward to the drain from the TQD in time  $t$ ,  $n_F(t)$ , and the number of electrons back transferred from the drain to the TQD in time  $t$ ,  $n_B(t)$ :

$$n(t) = n_F(t) - n_B(t), \quad (1)$$

where  $n(t)$  is commonly referred to as the jump number [61]. To incorporate the jump number into the dynamics of the open quantum system, we follow standard approaches and assume that there is a measuring device in the drain, where back-action is negligible, which records individual electron tunneling events. Since  $n(t)$  is a time-dependent stochastic variable, we actually seek the distribution of the total number of transferred electrons,  $P(n, t)$ .

We will connect  $P(n, t)$  to the system dynamics via  $\rho(t)$ , the reduced density matrix of the nanostructure. First, we resolve  $\rho(t)$  upon the jump number to define  $\rho^{(n)}(t)$ , the reduced density matrix of the nanostructure conditioned upon  $n$  electrons being recorded by the detector by time  $t$ . Considering that the general nanostructure states,  $\{|q\rangle\}$ , form a basis of the nanostructure subspace, then  $P(n, t)$  is

$$P(n, t) = \text{Tr}_q [\rho^{(n)}(t)]. \quad (2)$$

Included in  $V_D$  are measurement operators acting in the detector Hilbert space that increase,

$$\mathcal{M}^\dagger = \sum_{n=-\infty}^{\infty} |n\rangle\langle n-1|, \quad (7)$$

What remains now is to choose a method by which we can calculate  $\rho^{(n)}(t)$ ; we will use a BMME in the style of Li et al. [63, 64].

### A. General master equation

First, we decompose the total Hamiltonian into component parts,

$$H = H_Q + H_S + H_D + H_M + V, \quad (3)$$

where  $H_Q$  is the nanostructure Hamiltonian,  $H_S$  and  $H_D$  are the source and drain electrode Hamiltonians, respectively,  $V$  describes the nanostructure-electrode interaction, and  $H_M$  is the Hamiltonian of the measuring device, an electron detector in the drain. Section III introduces the specific TQD Hamiltonian, but for now let us consider the general nanostructure applied in Eq.(2) with the accompanying annihilation,  $a_q$ , and creation,  $a_q^\dagger$ , operators. Similarly, the detector Hamiltonian's exact form is not essential, but it can be generally written as

$$H_M = \sum_n \varepsilon_n |n\rangle\langle n|, \quad (4)$$

where  $|n\rangle$  is the state of the measurement device when the jump number is  $n$  at time  $t$ . The electrodes, modeled as non-interacting electrons, are denoted by  $\alpha \in \{S, D\}$ ,

$$H_\alpha = \sum_{\mathbf{k}_\alpha} \varepsilon_{\mathbf{k}_\alpha} a_{\mathbf{k}_\alpha}^\dagger a_{\mathbf{k}_\alpha}, \quad (5)$$

where the  $a_{\mathbf{k}_\alpha}$  and  $a_{\mathbf{k}_\alpha}^\dagger$  operators annihilate and create electrons in electrode  $\alpha$  with wavevector  $\mathbf{k}_\alpha$  and energy  $\varepsilon_{\mathbf{k}_\alpha}$ , respectively. The Hamiltonians of these individual parts together form  $H_0 = H_S + H_D + H_M + H_Q$ , the Hamiltonian of the uncoupled electrode-nanostructure-electrode system.

In contrast, the interaction Hamiltonian, which is composed of a source and drain contribution,  $V = V_S + V_D$ , contains the linear dynamics of electron tunneling across the configuration:

$$V = \sum_{\mathbf{k}_{S,q}} t_{\mathbf{k}_{S,q}} (a_{\mathbf{k}_S}^\dagger a_q + a_q^\dagger a_{\mathbf{k}_S}) + \sum_{\mathbf{k}_{D,q}} t_{\mathbf{k}_{D,q}} (\mathcal{M}^\dagger a_{\mathbf{k}_D}^\dagger a_q + \mathcal{M} a_q^\dagger a_{\mathbf{k}_D}) \quad (6)$$

and decrease,

$$\mathcal{M} = \sum_{n=-\infty}^{\infty} |n-1\rangle\langle n|, \quad (8)$$

the number of electrons detected by the measuring de-

vice, according to the corresponding drain tunneling operators.

Neglecting the nanostructure for the moment, let us consider the source, drain, and measuring device collectively as the bath, denoted by subscript “ $B$ ” and defined by the Hilbert space

$$B = S \otimes D \otimes M. \quad (9)$$

Alternatively, as Li et al. [63, 64] do, we can write the bath Hilbert subspace as a tensor product of the electrodes and many states of the detector,

$$B = \lim_{N \rightarrow \infty} B^{(-N)} \otimes \dots \otimes B^{(-1)} \otimes B^{(0)} \otimes B^{(1)} \otimes \dots \otimes B^{(N)}, \quad (10)$$

where  $B^{(n)} = S \otimes D \otimes |n\rangle\langle n|$  is the Hilbert space of the electrodes conditioned upon  $n$  electrons being detected by the measuring device.

Following from this bath-system demarcation, the reduced density matrix of the nanostructure is defined by tracing out the bath degrees of freedom from the total density matrix,  $\rho_T(t)$ :  $\rho(t) = \text{Tr}_B [\rho_T(t)]$ . Similarly, the  $n$ -resolved reduced density matrix of the nanostructure is

$$\rho^{(n)}(t) = \text{Tr}_{B^{(n)}} [\rho_T(t)] = \text{Tr}_B [|n\rangle\langle n| \rho_T(t)]. \quad (11)$$

Since the total density matrix of the system follows the Liouville-von Neumann equation of motion,

$$i \frac{d\rho_{T,I}}{dt} = [V_I(t), \rho_T(t)], \quad (12)$$

written here in the interaction picture, where operators are  $A_I(t) = e^{iH_0 t} A(t) e^{-iH_0 t}$ , we can obtain a time-evolution equation for the  $n$ -resolved reduced density matrix of the nanostructure as

$$\dot{\rho}_I^{(n)}(t) = - \int_0^t d\tau \text{Tr}_{B^{(n)}} [V_I(t), [V_I(t-\tau) \rho_{T,I}(t-\tau)]] . \quad (13)$$

In Eq.(13), we have expanded the Liouville-von Neuman equation to second-order in  $V_I(t)$  and performed the trace from Eq.(11).

Similarly to a standard BMME approach [65], we now expand the commutators in Eq.(13) and apply weak-coupling between the electrodes and the nanostructure. Rather than the regular Born approximation, however, this is enforced by assuming that the total density matrix follows the ansatz

$$\rho_T(t) \simeq \sum_{n=-\infty}^{\infty} \rho^{(n)}(t) \rho_S \rho_D |n\rangle\langle n|. \quad (14)$$

After leaving the interaction picture and then applying Markovianity, steps which are relegated to Appendix A for brevity, the master equation, written here in the basis of eigenstates of  $H_Q$ , is

$$\begin{aligned} i\dot{\rho}_{mn}^{(n)} &= \omega_{mn} \rho_{mn}^{(n)} + \sum_{qq'} \sum_{kl} \left( \sum_{\alpha} \left[ \Sigma_{\alpha}^{>}(\omega_{lk}) \langle m|a_q^{\dagger}|k\rangle \langle k|a_{q'}|l\rangle \rho_{ln}^{(n)} + \Sigma_{\alpha}^{<}(\omega_{kl})^* \langle m|a_q|k\rangle \langle k|a_{q'}^{\dagger}|l\rangle \rho_{ln}^{(n)} \right] \right. \\ &+ \Sigma_S^{<}(\omega_{nl}) \langle m|a_q^{\dagger}|k\rangle \rho_{kl}^{(n)} \langle l|a_{q'}|n\rangle + \Sigma_S^{>}(\omega_{ln})^* \langle m|a_q|k\rangle \rho_{kl}^{(n)} \langle l|a_{q'}^{\dagger}|n\rangle + \Sigma_D^{<}(\omega_{nl}) \langle m|a_q^{\dagger}|k\rangle \rho_{kl}^{(n+1)} \langle l|a_{q'}|n\rangle \\ &\left. + \Sigma_D^{>}(\omega_{ln})^* \langle m|a_q|k\rangle \rho_{kl}^{(n-1)} \langle l|a_{q'}^{\dagger}|n\rangle - (m \leftrightarrow n, k \leftrightarrow l)^* \right). \end{aligned} \quad (15)$$

Eq.(15) includes , we have introduced the lesser and greater self-energies of electrode  $\alpha$  as

$$\Sigma_{\alpha}^{<}(\omega) = \Delta_{\alpha}^{<}(\omega) + \frac{i}{2} \gamma^{\alpha} n_F(\omega - \mu_{\alpha}) \quad (16)$$

$$\Sigma_{\alpha}^{>}(\omega) = -\Delta_{\alpha}^{>}(\omega) - \frac{i}{2} \gamma^{\alpha} [1 - n_F(\omega - \mu_{\alpha})], \quad (17)$$

respectively, with real components given by the Lamb

shift,

$$\Delta_{\alpha}^{<}(\omega) = \frac{\gamma^{\alpha}}{2\pi} \lim_{\eta \rightarrow 0} \int_{-\infty}^{\infty} d\varepsilon \frac{(\varepsilon - \omega) n_F(\varepsilon - \mu_{\alpha})}{(\omega - \varepsilon)^2 + \eta^2} \quad (18)$$

$$\Delta_{\alpha}^{>}(\omega) = \frac{\gamma^{\alpha}}{2\pi} \lim_{\eta \rightarrow 0} \int_{-\infty}^{\infty} d\varepsilon \frac{(\varepsilon - \omega) [1 - n_F(\varepsilon - \mu_{\alpha})]}{(\omega - \varepsilon)^2 + \eta^2}, \quad (19)$$

and imaginary components given by the electrode-system coupling strength,

$$\gamma^{\alpha} = 2\pi |t_{\omega}|^2 \rho_{\alpha}, \quad (20)$$

where in Eq.(18)-Eq.(20) we have implicitly applied the wide-band limit and a constant density of states in the

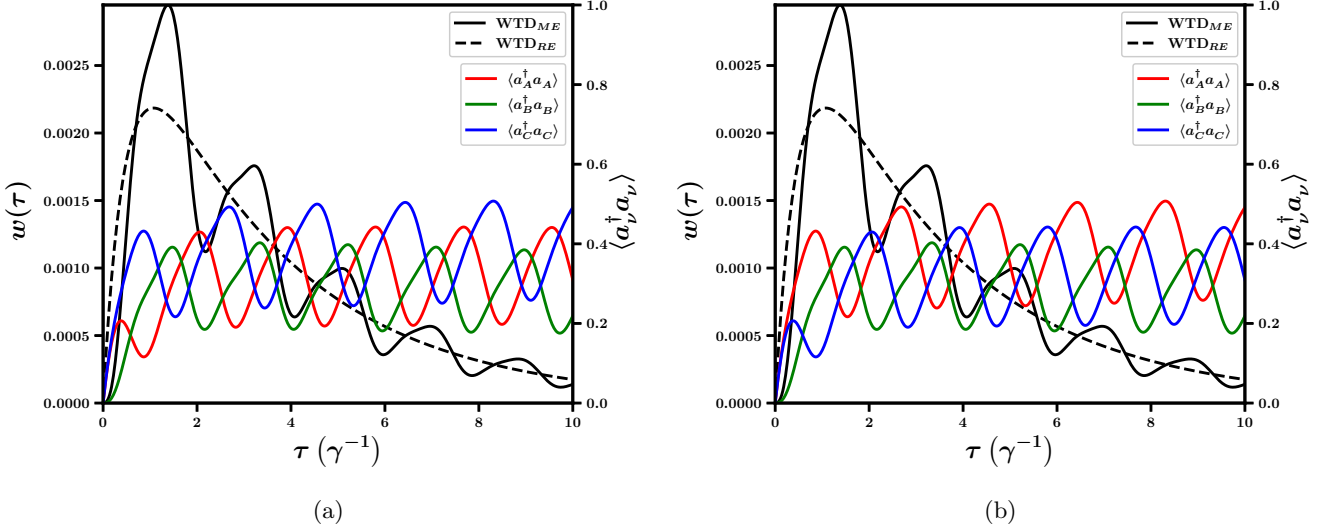


FIG. 2: WTD for the full BMME and rate equation (black) compared to the time-dependent dot occupation probabilities (multi-colored), for the configuration in Fig.(1a) and in the single-occupancy regime. The penetrating magnetic flux is  $\phi = \pm \frac{\pi}{2}$  for (a) and (b), respectively. Other parameters are:  $\varepsilon_B = 0$ ,  $\varepsilon_A = \Delta$ ,  $\varepsilon_C = -\Delta$ ,  $|t_{BC}| = |t_{AB}| = 2\gamma$ ,  $t_{AC} = 1.8\gamma$ ,  $T = 0.075\text{meV}$ ,  $\gamma = 0.01\text{meV}$ , and, in order to have unidirectional current,  $\mu_S = -\mu_D = 100\gamma$ .

electrodes. The self-energies also depend on the energy separation between eigenstates of  $H_Q$ :  $\omega_{mn} = E_m - E_n$ .

Under the wide-band limit, we can calculate the Lamb shifts analytically via residue theory and the digamma function  $\psi(x)$ :

$$\Delta_\alpha^<(\omega) = \frac{\gamma^\alpha}{2\pi} \Re \left\{ \psi \left( \frac{1}{2} + \frac{i}{2\pi T}(\omega - \mu_\alpha) \right) \right\} \quad (21)$$

$$\Delta_\alpha^>(\omega) = -\frac{\gamma^\alpha}{2\pi} \Re \left\{ \psi \left( \frac{1}{2} + \frac{i}{2\pi T}(\omega - \mu_\alpha) \right) \right\}. \quad (22)$$

Since the integrals in Eq.(18)-Eq.(19) are formally divergent, Eq.(21) and Eq.(22) also contain divergent log-

arithmic terms:  $-\lim_{W \rightarrow \infty} \ln \left[ \frac{W}{2\pi T} \right]$ . We can safely ignore these terms, however, because self-energies always appear in the master equation as pairs of differences,  $\Sigma_\alpha^<(\omega_{ij}) - \Sigma_\alpha^<(\omega_{kl})$ , so these terms will always cancel.

## B. Liouville space

In all practical calculations, we will actually work in Liouville space, rather than the Hilbert space of the TQD subsystem. To do so, we unfold  $\rho^{(n)}(t)$  from an  $N \times N$  density matrix to a vector,  $\mathbf{P}(n, t)$ , of length  $N^2$  and with the general form

$$\mathbf{P}(n, t) = \underbrace{[P_1(n, t), \dots, P_n(n, t), \dots, P_N(n, t)]}_{\text{Populations}} \left| \underbrace{[\rho_{12}(n, t), \dots, \rho_{mn}(n, t), \dots, \rho_{N, N-1}(n, t)]^T}_{\text{Coherences}} \right. \quad (23)$$

The population probability densities are  $P_k(n, t) = \rho_{kk}^{(n)}(t)$ . The trace, now, is defined as

$$\text{Tr} \left[ \rho^{(n)}(t) \right] = (\mathbf{I}, \mathbf{P}(n, t)), \quad (24)$$

where the round brackets denote an inner product and  $\mathbf{I} = [1, 1, \dots, 1, 0, 0, \dots, 0]$  is a row vector in which the first  $N$  elements are unity and the last  $N(N-1)$  elements are zero.

The probability vector in Eq.(23) obeys the time-

evolution equation

$$\begin{aligned} \dot{\mathbf{P}}(n, t) &= \sum_{n'} \mathbf{L}(n - n') \mathbf{P}(n, t) \\ &= \mathbf{L}_0 \mathbf{P}(n, t) + \mathbf{J}_F \mathbf{P}(n - 1, t) + \mathbf{J}_B \mathbf{P}(n + 1, t), \end{aligned} \quad (25)$$

which collects the dynamics described by the Markovian master equation from Eq.(15) into one ‘‘superoperator’’  $\mathbf{L}(n - n')$ : the Liouvillian. It is composed of  $\mathbf{J}_F$  and  $\mathbf{J}_B$ ,

quantum jump operators that describe tunneling to and from the drain, respectively, and  $\mathbf{L}_0 = \mathbf{L} - \mathbf{J}_F - \mathbf{J}_B$ , which contains the remaining dynamics. In order to calculate the FCS and WTD, it is expedient to perform a Fourier transform, introducing the counting field  $\chi$  [67, 68]:

$$\mathbf{P}(\chi, t) = \sum_{n=-\infty}^{\infty} e^{in\chi} \mathbf{P}(n, t), \quad (27)$$

$$\mathbf{P}(n, t) = \frac{1}{2\pi} \int_0^{2\pi} d\chi e^{-in\chi} \mathbf{P}(\chi, t). \quad (28)$$

Under this transformation, the time-evolution equation is

$$\dot{\mathbf{P}}(\chi, t) = \mathbf{L}(\chi) \mathbf{P}(\chi, t), \quad \text{where} \quad (29)$$

$$\mathbf{L}(\chi) = \mathbf{L}_0 + \mathbf{J}_F e^{i\chi} + \mathbf{J}_B e^{-i\chi}, \quad (30)$$

with solution

$$\mathbf{P}(\chi, t) = e^{\mathbf{L}(\chi)t} \bar{\mathbf{P}}, \quad (31)$$

assuming that all measurement starts in the stationary state, denoted by probability vector  $\bar{\mathbf{P}}$ .

### III. TQD MODELS AND TRANSPORT REGIMES

We perform all theory on a TQD arranged in either of the triangular geometries in Fig.(1a) and Fig.(1b). The three dots, to which we give the index  $\nu \in \{A, B, C\}$ , are each modeled with a single available orbital that is at most accessible to two electrons with opposite spin,  $\sigma \in \{\uparrow, \downarrow\}$ . The system Hamiltonian, for either geometry, is

$$H_Q = \sum_{\sigma} \sum_{\nu} \varepsilon_{\nu} a_{\nu, \sigma}^{\dagger} a_{\nu, \sigma} - \sum_{\nu \neq \nu'} t_{\nu \nu', \sigma} a_{\nu, \sigma}^{\dagger} a_{\nu', \sigma} + \sum_{\nu} U_{\nu \nu} n_{\nu, \uparrow} n_{\nu, \downarrow} + \sum_{\nu < \nu'} \sum_{\sigma \sigma'} U_{\nu \nu'} n_{\nu, \sigma} n_{\nu', \sigma'}. \quad (32)$$

where  $\varepsilon_{\nu}$  is the energy of each dot,  $U_{\nu \nu}$  and  $U_{\nu \nu'}$  are the intra- and inter-dot Coulomb repulsions, respectively, and  $t_{\nu \nu'} = t_{\nu' \nu}^*$  is the hopping parameter for tunneling from dot  $\nu'$  to dot  $\nu$ . As usual, the  $a_{\nu, \sigma}^{\dagger}$  and  $a_{\nu, \sigma}$  operators create and annihilate an electron on dot  $\nu$  with energy  $\varepsilon_{\nu}$  and spin  $\sigma$ , respectively, while  $n_{\nu, \sigma} = a_{\nu, \sigma}^{\dagger} a_{\nu, \sigma}$  is the corresponding particle number operator. Aharonov-Bohm interference interacts with the dynamics by inducing a phase difference,  $\phi$ , between different paths around the TQD:  $\phi = \oint \mathbf{A} \cdot d\ell = 2\pi\Phi/\Phi_0$ , where  $\mathbf{A}$  is the magnetic

vector potential and  $\Phi_0 = \frac{h}{e}$  is the magnetic flux quantum [69]. In all calculations, we choose a gauge where the phase difference between the two paths is factored entirely onto the coupling between dot  $A$  and dot  $C$ :  $t_{AC} = |t_{AC}| e^{i\phi}$ , with  $t_{AB}$  and  $t_{BC}$  always real.

For the configuration in Fig.(1a), where both the  $A$  and  $C$  dots are coupled to the source and the  $B$  dot alone is coupled to the drain, the interaction Hamiltonian is

$$V = \sum_{\mathbf{k}_S} \sum_{\nu=\{A,C\}} t_{\mathbf{k}_S, \nu, \sigma} \left( a_{\mathbf{k}_S, \nu, \sigma}^{\dagger} a_{\nu, \sigma} + a_{\nu, \sigma}^{\dagger} a_{\mathbf{k}_S} \right) + \sum_{\mathbf{k}_D} t_{\mathbf{k}_D, B, \sigma} \left( \mathcal{M}^{\dagger} a_{\mathbf{k}_D}^{\dagger} a_{B, \sigma} + \mathcal{M} a_{B, \sigma}^{\dagger} a_{\mathbf{k}_D} \right). \quad (33)$$

Conversely, the interaction Hamiltonian for the config-

uration in Fig.(1b), where the  $B$  dot is coupled to the source and the  $A$  and  $C$  dots are coupled to the drain, is

$$V = \sum_{\mathbf{k}_D} \sum_{\nu=\{A,C\}} t_{\mathbf{k}_D, \nu, \sigma} \left( \mathcal{M}^{\dagger} a_{\mathbf{k}_D}^{\dagger} a_{\nu, \sigma} + \mathcal{M} a_{\nu, \sigma}^{\dagger} a_{\mathbf{k}_D} \right) + \sum_{\mathbf{k}_S} t_{\mathbf{k}_S, B, \sigma} \left( a_{\mathbf{k}_S}^{\dagger} a_{B, \sigma} + a_{B, \sigma}^{\dagger} a_{\mathbf{k}_S} \right). \quad (34)$$

At this point in the theory, we cannot apply the TQD

Hamiltonian defined in Eq.(32) to the  $n$ -resolved mas-

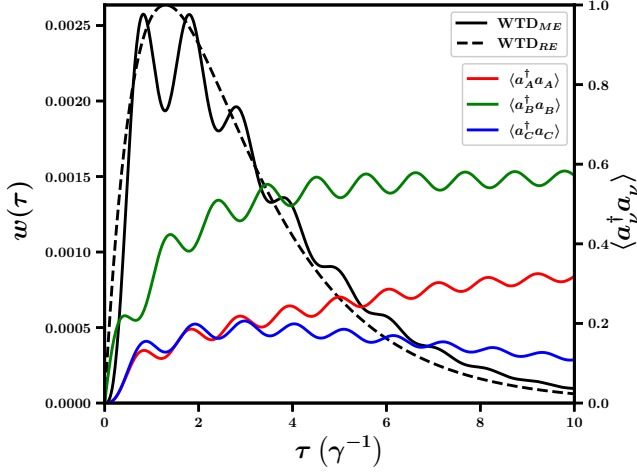


FIG. 3: WTD and occupation probabilities for the reverse configuration in Fig.(1a). All parameters are the same as in Fig.(2a) and Fig.(2b), except for the magnetic flux, which is now  $\phi = \pi$ .

ter equation, because it is written in the basis of dot states and is consequently not diagonal. Although for restrictive transport regimes there exist analytic diagonalizations of the TQD Hamiltonian [39], we can always numerically diagonalize  $H_Q$  via its eigenstates:

$$\begin{aligned} \tilde{H}_Q &= \sum_{kk'} |m_k\rangle \langle m_k| H_Q |m_{k'}\rangle \langle m_{k'}| \\ &= \sum_{k=1}^N E_k |m_k\rangle \langle m_k|, \end{aligned} \quad (35)$$

where  $E_k$  is the eigenenergy of eigenstate  $|m_k\rangle$ . We can also write the dot states,  $|d_i\rangle$ , in the new basis,

$$|d_i\rangle = \sum_{k=1}^N |m_k\rangle \langle m_k| d_i\rangle, \quad (36)$$

and, since the dot states also span the system space, compute the inverse transformation:

$$|m_k\rangle = \sum_{i=1}^N |d_i\rangle \langle d_i| m_k\rangle. \quad (37)$$

With no parameter restrictions, however, the full Fock space is quite large and numerical diagonalization is a formidable task. There can be a maximum of six electrons occupying the configuration, so  $N = \sum_{k=0}^6 \frac{6!}{k!(6-k)!} = 64$  and the resulting density matrix has 4096 elements. To reduce the complexity and computational requirements, many theoretical investigations instead focus on limiting regimes where the dimensionality is much smaller [39–41]; several of which we will consider here.

### A. Spin-independent triple and single-occupancy

In the first transport scenario, we assume that the intra-dot Coulomb repulsion is large:  $U_{\nu\nu} \rightarrow \infty$ . Under this limit, each dot in the configuration can be occupied by only one excess electron, which we label the *triple-occupancy* regime. Spanning the system are ten dot states: the configuration can be empty,  $|0\rangle$ ; a single electron may occupy any of the three dots,  $|A\rangle$ ,  $|B\rangle$ , or  $|C\rangle$ ; two electrons may be occupying any two of the dots,  $|AB\rangle$ ,  $|AC\rangle$ , or  $|BC\rangle$ ; or all three dots are occupied,  $|ABC\rangle = |3\rangle$ .

Although  $|0\rangle$  and  $|3\rangle$  are invariant under the diagonalization, the transformed basis has three new single-occupancy,

$$|1i\rangle = c_{1i,A}|A\rangle + c_{1i,B}|B\rangle + c_{1i,C}|C\rangle \quad (38)$$

and double-occupancy,

$$|2i\rangle = c_{2i,AB}|AB\rangle + c_{2i,AC}|AC\rangle + c_{2i,BC}|BC\rangle, \quad (39)$$

states, where  $i = 1, 2, 3$ . From Eq.(37), the coefficients are evidently  $c_{1i,\nu} = \langle \nu | 1i\rangle$  and  $c_{2i,\nu\nu'} = \langle \nu\nu' | 2i\rangle$ . In addition to this large reduction in dimensionality, all eigenstates with different electron occupancy are orthogonal and thus decouple in the master equation; the remaining 20 elements unfold into the probability vector

$$\begin{aligned} \mathbf{P}(\chi, t) &= [P_0(\chi, t), P_{11}(\chi, t), P_{12}(\chi, t), P_{13}(\chi, t), P_{21}(\chi, t), P_{22}(\chi, t), P_{23}(\chi, t), P_3(\chi, t), \\ &\quad \rho_{11,12}(\chi, t), \rho_{11,13}(\chi, t), \rho_{12,13}(\chi, t), \rho_{12,11}(\chi, t), \rho_{13,11}(\chi, t), \rho_{13,12}(\chi, t), \\ &\quad \rho_{21,22}(\chi, t), \rho_{21,23}(\chi, t), \rho_{22,23}(\chi, t), \rho_{22,21}(\chi, t), \rho_{23,21}(\chi, t), \rho_{23,22}(\chi, t)]^T. \end{aligned} \quad (40)$$

After applying a Fourier transform to Eq.(15), as well

as the rotating wave approximation so that  $q \neq q'$  terms

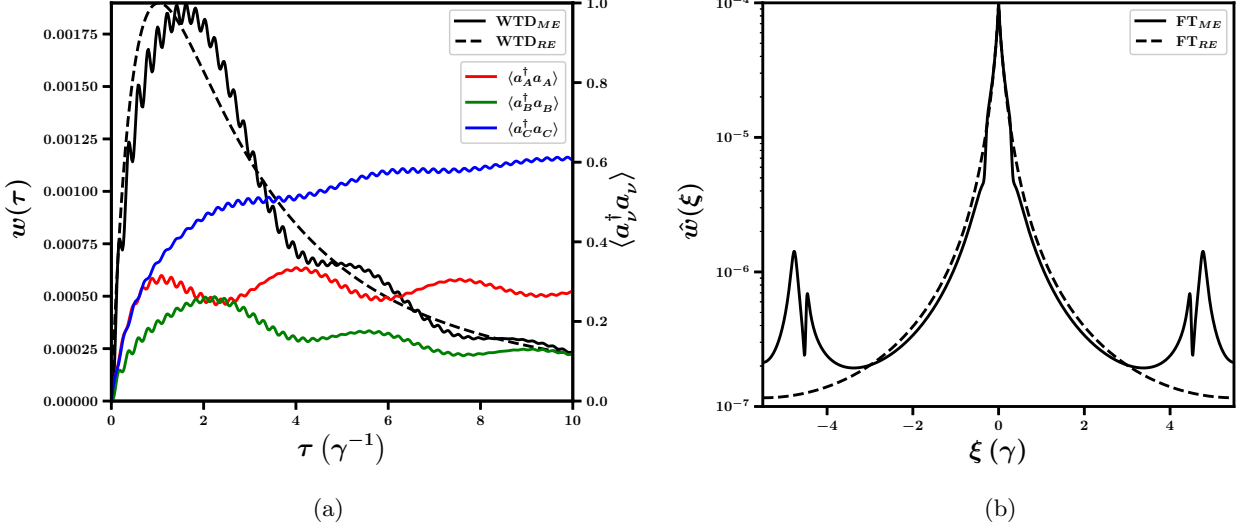


FIG. 4: WTD and occupation probabilities (a) and the corresponding Fourier transform of the WTD,  $\hat{w}(\xi)$ , (b) for the same parameters as in Fig.(2a) and Fig.(2b), except that now  $\phi = \pi$  and the inter-dot couplings are much stronger:  $|t_{AB}| = |t_{BC}| = 10\gamma$  and  $|t_{AC}| = 9\gamma$ .

are neglected, the master equation is

$$\begin{aligned}
\dot{\rho}_{mn}(\chi, t) = & -i\omega_{mn}\rho_{mn}(\chi, t) - i \sum_{k\ell} \left[ \sum_{\nu=\{A,C\}} \left( \Sigma_S^<(\omega_{k\ell})^* \langle m|a_\nu|k \rangle \langle k|a_\nu^\dagger|\ell \rangle \rho_{\ell n} + \Sigma_S^>(\omega_{\ell k}) \langle m|a_\nu^\dagger|k \rangle \langle k|a_\nu|\ell \rangle \rho_{\ell n} \right. \right. \\
& + \Sigma_S^<(\omega_{n\ell}) \langle m|a_\nu^\dagger|k \rangle \rho_{k\ell} \langle \ell|a_\nu|n \rangle + \Sigma_S^>(\omega_{\ell n}) \langle m|a_\nu|k \rangle \rho_{k\ell} \langle \ell|a_\nu^\dagger|n \rangle - \Sigma_S^<(\omega_{\ell k}) \rho_{mk} \langle k|a_\nu|\ell \rangle \langle \ell|a_\nu^\dagger|n \rangle \\
& - \Sigma_S^>(\omega_{k\ell})^* \rho_{mk} \langle k|a_\nu^\dagger|\ell \rangle \langle \ell|a_\nu|n \rangle - \Sigma_S^<(\omega_{mk})^* \langle m|a_\nu^\dagger|k \rangle \rho_{k\ell} \langle \ell|a_\nu|n \rangle - \Sigma_S^>(\omega_{km}) \langle m|a_\nu|k \rangle \rho_{k\ell} \langle \ell|a_\nu^\dagger|n \rangle \left. \right) \\
& + \Sigma_D^<(\omega_{k\ell})^* \langle m|a_B|k \rangle \langle k|a_B^\dagger|\ell \rangle \rho_{\ell n} + \Sigma_D^>(\omega_{\ell k}) \langle m|a_B^\dagger|k \rangle \langle k|a_B|\ell \rangle \rho_{\ell n} + \Sigma_D^<(\omega_{n\ell}) e^{-i\chi} \langle m|a_B^\dagger|k \rangle \rho_{k\ell} \langle \ell|a_B|n \rangle \\
& + \Sigma_D^>(\omega_{\ell n})^* e^{i\chi} \langle m|a_B|k \rangle \rho_{k\ell} \langle \ell|a_B^\dagger|n \rangle - \Sigma_D^<(\omega_{\ell k}) \rho_{mk} \langle k|a_B|\ell \rangle \langle \ell|a_B^\dagger|n \rangle - \Sigma_D^>(\omega_{k\ell})^* \rho_{mk} \langle k|a_B^\dagger|\ell \rangle \langle \ell|a_B|n \rangle \\
& \left. - \Sigma_D^<(\omega_{mk})^* e^{-i\chi} \langle m|a_B^\dagger|k \rangle \rho_{k\ell} \langle \ell|a_B|n \rangle - \Sigma_D^>(\omega_{km}) e^{i\chi} \langle m|a_B|k \rangle \rho_{k\ell} \langle \ell|a_B^\dagger|n \rangle \right]. \quad (41)
\end{aligned}$$

The corresponding master equation for the configuration in Fig.(1b) is similar, except that the drain self-energies now lie under the summation of  $A, C$ , and the source self-energies do not. For triple-occupancy, there are four types of coupled density matrix elements,  $\rho_{0,0}$ ,  $\rho_{1i,1j}$ ,  $\rho_{2i,2j}$ , and  $\rho_{3,3}$ , which we display in Appendix B.

If we also take the inter-dot repulsion as large,  $U_{\nu\nu'} \rightarrow \infty$ , then only one dot may be occupied at a time: the *single-occupancy* regime. In this case, the probability vector is much smaller,

$$\begin{aligned}
\mathbf{P}(\chi, t) = & [P_0(\chi, t), P_{11}(\chi, t), P_{12}(\chi, t), P_{13}(\chi, t), \\
& \rho_{11,12}(\chi, t), \rho_{11,13}(\chi, t), \rho_{12,13}(\chi, t), \\
& \rho_{12,11}(\chi, t), \rho_{13,11}(\chi, t), \rho_{13,12}(\chi, t)]^T, \quad (42)
\end{aligned}$$

and analytic solutions are available [39].

## B. Spin-dependent double-occupancy

In the *double-occupancy* regime, the intra-dot Coulomb repulsion is finite, but the inter-dot repulsion is large;  $U_{\nu\nu'} \rightarrow \infty$  and each dot can be occupied by two electrons of opposite spin, but only two electrons are allowed in the entire TQD configuration. There are now 6 single electron states and 15 double electron states, for a total of 22 states spanning the system and 262 coupled density matrix elements. To simplify, we also assume a large bias voltage,  $V_{SD} \rightarrow \infty$ , so that tunneling can only be from the source to the TQD or from the TQD to the drain, and high temperature limit, so that we can use a Lindblad

master equation. For the configuration in Fig.(1a) this is

$$\begin{aligned} \frac{d\rho}{dt} = & -i[H_Q, \rho] + \\ & \sum_{\sigma, \nu \in \{A, C\}} \gamma^S \left( a_{\nu, \sigma}^\dagger \rho a_{\nu, \sigma} - \frac{1}{2} a_{\nu, \sigma} a_{\nu, \sigma}^\dagger \rho - \frac{1}{2} \rho a_{\nu, \sigma} a_{\nu, \sigma}^\dagger \right) + \\ & \sum_{\sigma} \gamma^D \left( a_{B, \sigma} \rho a_{B, \sigma}^\dagger e^{i\chi} - \frac{1}{2} a_{B, \sigma}^\dagger a_{B, \sigma} \rho - \frac{1}{2} \rho a_{B, \sigma}^\dagger a_{B, \sigma} \right), \end{aligned} \quad (43)$$

and for the configuration in Fig.(1b) we exchange  $\nu \in \{A, C\} \leftrightarrow B$  and  $\gamma^S \leftrightarrow \gamma^D$ .

We are justified in making this final assumption because all results are calculated from the WTD, which requires unidirectional tunneling and, therefore, a large bias voltage.

## IV. FLUCTUATION STATISTICS

### A. Full counting statistics

The FCS are cumulants of the distribution of total current,  $\langle\langle I^k \rangle\rangle$ , and can easily be derived from the distribution of total transferred charge as long as  $P(n, t)$  satisfies a large deviation principle [70]. In this case, cumulants of  $P(n, t)$  scale linearly in time,

$$\langle\langle n(t)^k \rangle\rangle \approx \langle\langle I^k \rangle\rangle t, \quad (44)$$

and the current cumulants are the asymptotic growth rates:

$$\lim_{t \rightarrow \infty} \langle\langle I(t)^k \rangle\rangle = e^k \frac{d}{dt} \langle\langle n(t)^k \rangle\rangle \quad (45)$$

$$\approx \langle\langle I^k \rangle\rangle. \quad (46)$$

In this large deviation, or long-time limit, Bagrets and Nazarov [67] have shown that the cumulant generating function of  $P(n, t)$  is

$$\lim_{t \rightarrow \infty} K(\chi, t) = t \Lambda_{\max}(\chi), \quad (47)$$

where  $\Lambda_{\max}(\chi)$  is the eigenvalue of  $\mathbf{L}(\chi)$  with the largest real part. Combining Eq.(44) and Eq.(47) yields the zero-frequency current cumulants:

$$\langle\langle I^k \rangle\rangle = (-i)^k \left. \frac{\partial^k}{\partial \chi^k} \Lambda_{\max} \right|_{\chi=0}. \quad (48)$$

The fluctuation statistics of triangular TQDs have largely focused on the current cumulants as defined above, and in particular on the Fano factor,  $F$ , which scales the noise to that of a Poissonian process. It is defined from the first cumulant, the average stationary current  $\langle I \rangle$ , and the second cumulant, which is related to the zero-frequency noise as  $\langle\langle I^2 \rangle\rangle = \frac{1}{2} \mathcal{S}(0)$ :

$$F = \frac{\mathcal{S}(0)}{2\langle I \rangle} = \frac{\langle\langle I^2 \rangle\rangle}{\langle I \rangle}. \quad (49)$$

### B. Waiting time distribution

We will also examine the fluctuation statistics of the TQD models in Fig.(1a) and Fig.(1a) with a fluctuating-time approach, the WTD, which has received only limited theoretical attention [1, 62]. In the context of electron transport through the general electrode-nanostructure-electrode paradigm we are using, the WTD is defined as the probability density that two quantum jumps are separated by a time delay  $\tau$ , conditioned on the probability density of the initial quantum jump.

In the stationary state and in the limit of unidirectional tunneling, the distribution of waiting times between successive jumps to the drain is

$$w(\tau) = \frac{(\mathbf{I}, \mathbf{J}_D^F e^{(\mathbf{L} - \mathbf{J}_D^F)\tau} \mathbf{J}_D^F \bar{\mathbf{P}})}{(\mathbf{I}, \mathbf{J}_D^F \bar{\mathbf{P}})}, \quad (50)$$

where  $\mathbf{J}_D^F$  is the quantum jump operator [48] containing all transitions from the system to the drain. It naturally contains all terms with an  $e^{i\chi}$  attached to them in Eq.(15).

To compare to the FCS, we will need to use the waiting time cumulants, defined from the WTD Laplace transform,

$$\tilde{w}(z) = \int_0^\infty d\tau e^{z\tau} w(\tau) \quad (51)$$

$$= \frac{(\mathbf{I}, \mathbf{J}_l [z - (\mathbf{L} - \mathbf{J}_D^F)]^{-1} \mathbf{J}_D^F \bar{\mathbf{P}})}{(\mathbf{I}, \mathbf{J}_D^F \bar{\mathbf{P}})}, \quad (52)$$

which conveniently defines a cumulant generating function:

$$\langle\langle \tau^k \rangle\rangle = (-1)^k \left. \frac{d^k}{dz^k} \ln \tilde{w}(z) \right|_{z=0}. \quad (53)$$

Apart from the standard WTD in Eq.(50), to calculate correlations we will also need the second-order WTD  $w(\tau_1, \tau_2)$ :

$$w(\tau_1, \tau_2) = \frac{(\mathbf{I}, \mathbf{J}_D^F e^{(\mathbf{L} - \mathbf{J}_D^F)\tau_2} \mathbf{J}_D^F e^{(\mathbf{L} - \mathbf{J}_D^F)\tau_1} \mathbf{J}_D^F \bar{\mathbf{P}})}{(\mathbf{I}, \mathbf{J}_D^F \bar{\mathbf{P}})}, \quad (54)$$

alongside the second-order average waiting time

$$\langle\langle \tau_1 \tau_2 \rangle\rangle = \left. \frac{\partial}{\partial z_1} \frac{\partial}{\partial z_2} \ln \tilde{w}(z_1, z_2) \right|_{z_1=z_2=0}. \quad (55)$$

### C. Renewal and non-renewal theory

The WTD is a useful theoretical tool to compare alongside the FCS because it provides information on short-time physics that the large deviation limit of the FCS does not. As an example, correlations between successive waiting times  $\tau$  and  $\tau_2$  imply that the system does

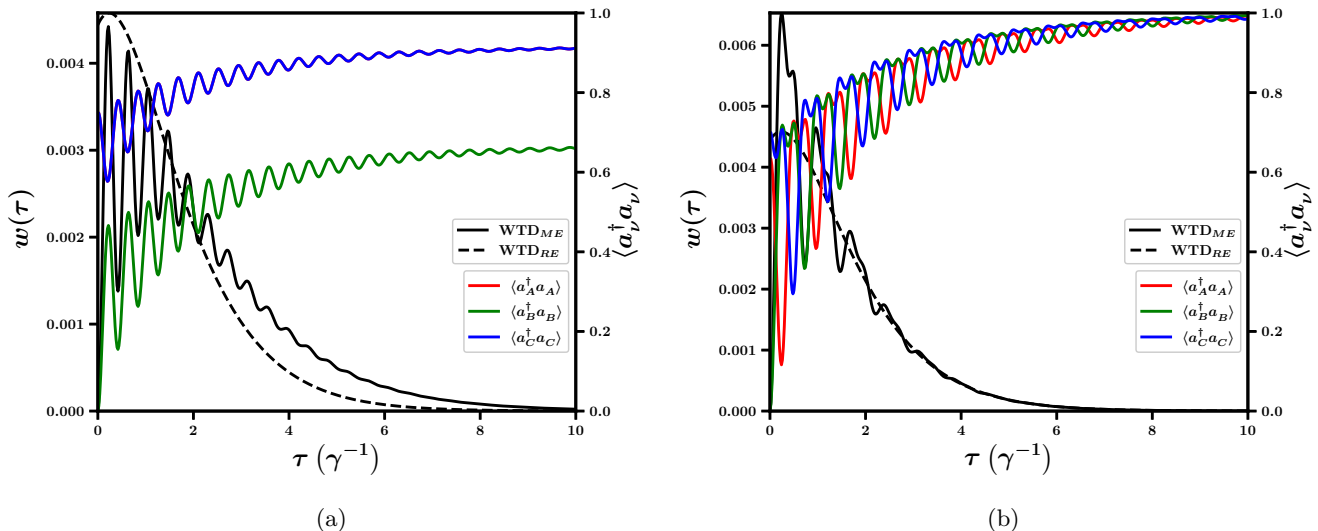


FIG. 5: WTD and occupation probabilities for the configuration in the triple-occupancy regime for the configuration in Fig.(1a). Magnetic flux is  $\phi = \pi$  in (a) and  $\phi = \frac{\pi}{2}$  in (b). The inter-dot interaction is  $U_{\nu\nu'} = \gamma$ , all inter-dot couplings are set to  $|t| = 5\gamma$ , and all other parameters remain the same as in previous plots.

not entirely ‘renew’ itself after each tunneling, and are indicative of non-trivial underlying transport dynamics [59, 60, 71–75]. Waiting time correlations are largely studied via the linear Pearson correlation coefficient:

$$p = \frac{\langle \tau_1 \tau_2 \rangle - \langle \tau \rangle^2}{\langle \tau^2 \rangle}, \quad (56)$$

where  $\langle \tau_1 \tau_2 \rangle$  is calculated from the joint WTD  $w(\tau_1, \tau_2)$ . The Pearson correlation coefficient, roughly speaking, calculates an average of waiting time correlations over the entire landscape of  $\tau_1$  and  $\tau_2$ . While useful, this approach can wash out non-zero correlations occurring only for specific regimes of  $\tau_1$  and  $\tau_2$ , potentially obscuring important information. Consequently, we will also calculate the quantity

$$W(\tau_1, \tau_2) = \frac{w(\tau_1, \tau_2) - w(\tau_1)w(\tau_2)}{w(\tau_1)w(\tau_2)}, \quad (57)$$

which describes correlations for each combination of  $\tau_1$  and  $\tau_2$ .  $W(\tau_1, \tau_2)$  is interpreted thus: given a pair of successive waiting times  $\tau_1$  and  $\tau_2$ , if the corresponding  $W(\tau_1, \tau_2)$  is positive (negative) then it is likely (unlikely) to observe this pair compared to others. If  $W(\tau_1, \tau_2) \approx 0$ , however, then this pair is no more likely or unlikely to be observed than any other.

## V. RESULTS

### A. Spin-independent single-occupancy

The single-occupancy case, in which the TQD can only be occupied by one excess electron, has received great

theoretical attention due to the analytic solutions available in this regime. At  $\phi = 0$ , for example, Emory [39] showed that energy parameters for the configuration in Fig.(1a) can always be adjusted to produce a coherent superposition of dots  $A$  and  $C$ , in which case the dot  $B$  occupancy is blocked:

$$|\Psi\rangle = \frac{1}{\sqrt{t_{AC}^2 + t_{BC}^2}} (t_{BC}|A\rangle - t_{AB}|C\rangle). \quad (58)$$

Here,  $|\Psi\rangle$ , known as a ‘‘dark state’’, is an eigenvector of  $H_Q$ . To achieve Eq.(58), the required parameter choices are  $\varepsilon_B = 0$ ,  $\varepsilon_A = \Delta$ , and  $\varepsilon_C = -\Delta$ , where

$$\Delta = \frac{|t_{AC}|}{2|t_{AB}||t_{CB}|} (|t_{AB}|^2 - |t_{CB}|^2). \quad (59)$$

Unsurprisingly, he found that formation of a dark state is generally accompanied by super-Poissonian noise, attributed to avalanche tunneling caused by the coherent population blocking. Although super-Poissonian noise is often a symptom of underlying time-correlations, such as when a system displays telegraphic switching [74, 75], in this case renewal theory yields no extra information about the dynamics.

Because we are limiting the TQD to only one excess electron, the transport in this regime is effectively single-reset; once the TQD empties via a tunneling to the drain, another electron must tunnel in from the source before the next jump to the drain. While each tunneling electron can coherently interfere with itself, therefore, it cannot interfere with other tunneling electrons and the Pearson coefficient is zero for all parameter choices. The single-reset nature is evident in all corresponding WTD plots, such as Fig.(2a), where  $w(0) = 0$ . Even

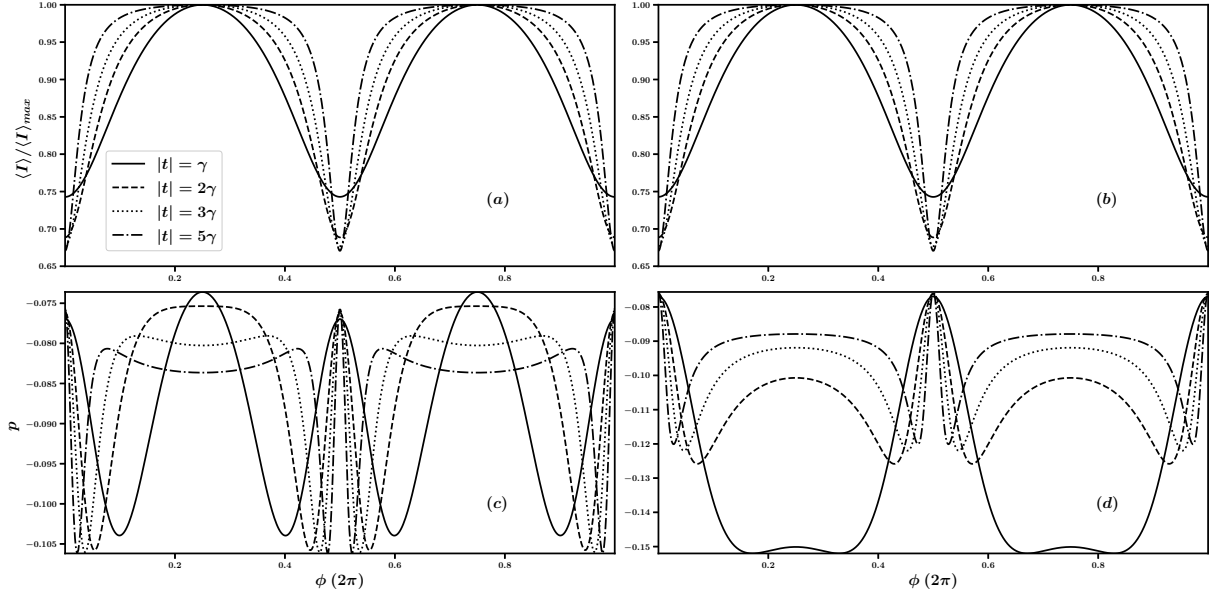


FIG. 6: Current as a proportion of its maximum, (a) and (b), and corresponding Pearson correlation coefficient, (c) and (d), all as a function of penetrating magnetic flux  $\phi$  and in the triple-occupancy regime for various  $|t|$ . As in Figs.(5a)-(5b), the inter-dot couplings are all equal to  $|t|$  and  $U_{\nu\nu'} = \gamma$ ; otherwise we use the same parameters as all previous plots. The left column is calculated for the configuration in Fig.(1a) and the right column for its mirror in Fig.(1b).

though there are no time-correlated dynamics, however, the WTD itself still provides useful information about the single-occupancy regime.

As seen in Figs.(2a)-(4b), the WTD calculated from the BMME displays periodic oscillations which, since they disappear in the WTD calculated from the rate equation, must originate from phase factors due to coherent transport. In these figures we have also plotted the time-dependent average occupancies of each dot after a tunneling to the drain,

$$\langle a_\nu^\dagger a_\nu \rangle = \text{Tr} [a_\nu^\dagger a_\nu \rho(t)], \quad \text{with} \quad (60)$$

$$\rho(t) = \frac{(\mathbf{I}, e^{(\mathbf{L} - \mathbf{J}_D^F)\tau} \mathbf{J}_D^F \bar{\mathbf{P}})}{(\mathbf{I}, \mathbf{J}_D^F \bar{\mathbf{P}})}, \quad (61)$$

because, as Engelhardt and Cao found, we can correlate WTD behavior to the relevant dot occupancies [1]. In the configuration where only dot  $B$  is coupled to the drain, for example, the WTD remains in phase with the time-dependent occupation of dot  $B$ , which is shown in Fig.(2a) and Fig.(2b). Interestingly, while it may not be immediately obvious, on close inspection it is evident that each WTD peak in these plots has two components: one from the corresponding peak in  $\langle a_B^\dagger a_B \rangle$  and one from a peak in  $\langle a_C^\dagger a_C \rangle$  for Fig.(2a) and  $\langle a_A^\dagger a_A \rangle$  for Fig.(2b). Since a peak in the WTD must correspond to occupation of dot  $B$ , this second smaller contribution must correspond to a coherent single-electron state formed between  $B$  and either  $A$  or  $C$ . The choice is evidently determined by the sign of the magnetic flux; in Fig.(2a), the phase

shift is positive,  $\phi = +\frac{\pi}{2}$ , and the electron moves anti-clockwise from  $C \rightarrow B \rightarrow A$ , while in Fig.(2a), the phase shift is negative,  $\phi = -\frac{\pi}{2}$ , and the electron moves clockwise from  $A \rightarrow B \rightarrow C$  [1].

In Fig.(3), which displays the WTDs and occupancies for the configuration in Fig.(1b), we can apply the same analysis. Here, dots  $A$  and  $C$  are coupled to the drain, so the WTD peaks correspond to peaks in the occupancies of these two dots. Of note here are that the WTD is bimodal; since dot  $B$  is coupled to dots  $A$  and  $C$  equally and the magnetic flux is  $\phi = \pi$ , there are two equally probable paths to the drain for the electron to take after entering from the source. At later times, by contrast, the asymmetric dot coupling and energy difference between the levels,  $\varepsilon_A - \varepsilon_C = 2\Delta$ , causes the occupancy of dot  $A$  to correspond with the WTD more closely.

The final single-occupancy case we consider is that of large inter-dot coupling:  $|t| \sim 10\gamma$  in Fig.(4a). For such coupling, the electron is strongly hybridized across the three dots, and so undergoes many inter-dot transitions between tunnelings to the drain. This results in distinct global WTD oscillations, occurring with period  $\sim 4\gamma^{-1}$ , supplemented by small local oscillations with period  $\sim 0.2\gamma^{-1}$ . From the corresponding Fourier transform of the WTD,  $\hat{w}(\xi)$ , which is plotted in Fig.(4b) on a logscale, we see that the small local oscillations are actually resolved into two frequencies at  $4.8\gamma = |t_{AC}|/2$  and  $5\gamma = |t_{AB}|/2, |t_{BC}|/2$ , which evidently correspond to inter-dot transitions. Although not shown, when all  $|t_{\nu\nu'}|$  are equal, this double peak collapses into one. The

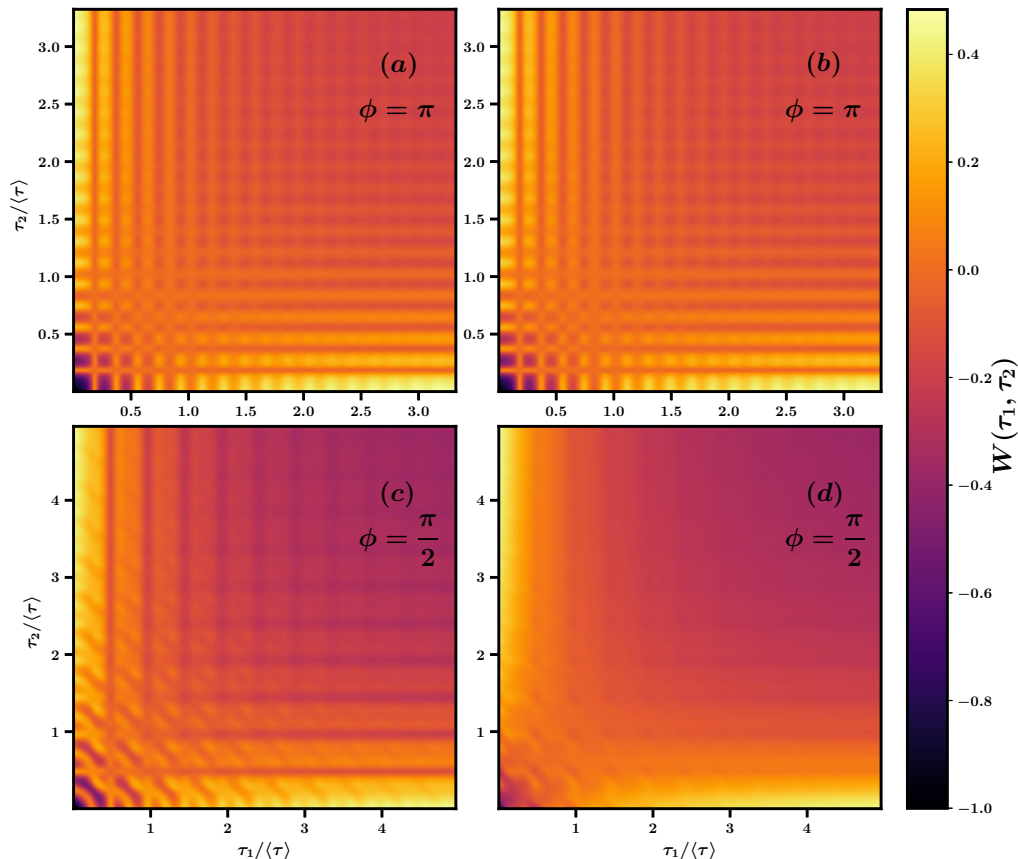


FIG. 7:  $W(\tau_1, \tau_2)$  for multiple configurations and magnetic flux. As in Fig.(6), the columns are organized with Fig.(1a) on the left and Fig(1b) on the right, while the two rows set magnetic flux to  $\phi = \pi$  and  $\phi = \frac{\pi}{2}$ , respectively. Inter-dot dot couplings are  $|t| = 5\gamma$ , and all other parameters are the same as in Fig.(6).

global WTD oscillations, on the other hand, originate from a frequency at  $xi \approx 0.25\gamma$ ; it is not yet clear what dynamics produces this behavior and this remains an interesting open question for us.

### B. Spin-independent triple-occupancy

In the spin-independent triple-occupancy regime, the TQD may be occupied by three excess electrons, but there can only be one excess electron on each dot. Unlike the single-occupancy regime, to observe coherent oscillations now requires an inter-dot coupling greater than the coupling between the TQD and the electrodes:  $|t| > \gamma$ . If  $|t| \sim \gamma$ , then the second tunneling to the drain will happen on the same time-scale as transitions between the dots; the resulting WTD is single-peaked. Accordingly, in Figs.(5a)-(5b), we have set  $|t| = 5\gamma$ .

Although the resulting Fock space is now more complicated, we can still draw relationships between the WTD and corresponding dot occupations as we did for the single-occupancy regime. In Fig.(5a), for example, os-

cillations in the WTD again correspond to oscillations in the dot  $B$  occupancy, which occur at periodic minima in both the  $A$  and  $C$  dot occupancies, as this is for the configuration in Fig.(1a). Since  $\phi = \pi$  and the dot couplings are symmetric, furthermore, the  $A$  and  $C$  dot occupancies remain in phase at all times. By contrast, Fig.(5b) sets  $\phi = \frac{\pi}{2}$ ; the Aharonov-Bohm phase now introduces multiple frequencies into the coherent oscillations and separates the  $A$  and  $C$  occupancies. Apart from the absence of coherent oscillations, in this regime, the rate equation WTD includes another quantitative discrepancy; it predicts that the transport is multiple-reset,  $w(\tau) \neq 0$ , indicating that dot  $B$  can be occupied by more than one electron. The BMME WTD, however, captures the correct behavior.

Despite using the same parameters in Figs.(5a)-(5b) that produced a dark state in the single-occupancy regime, the presence of three electrons largely lifts the coherent population blocking. This can be observed in Figs.(6a)-(6b), which calculate the stationary current as a function of the penetrating magnetic flux for both TQD configurations. Similarly to the single-occupancy regime, the current displays Aharonov-Bohm oscillations, but

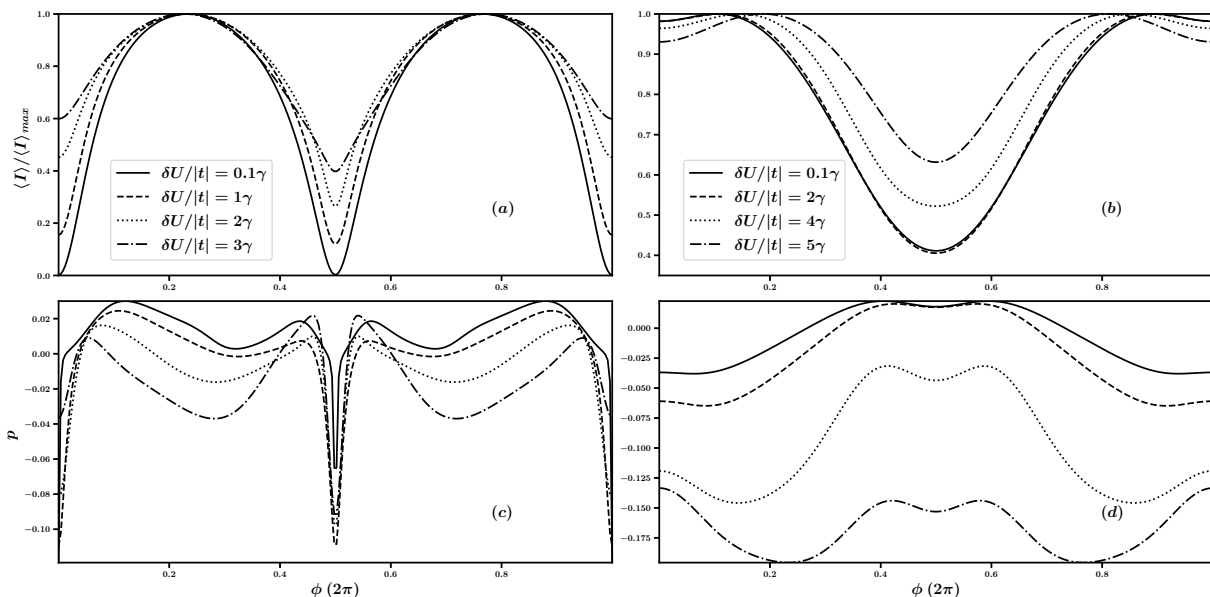


FIG. 8: Current as a proportion of its maximum, (a) and (b), and the corresponding Pearson correlation coefficient, (c) and (d), as a function of  $\phi$  and for different  $\delta U/|t|$ . As before, the left column is calculated for the Fig.(1a) configuration and the right column for the Fig.(1b) configuration. All dot energies are set to  $\varepsilon_\nu = 0$ , inter-dot couplings are all  $|t| = \gamma$ , the inter-dot Coulomb interactions are  $U_{AC} = 10\gamma$  and  $U_{AB} = U_{BC} = 11\gamma$ , and the intra-dot Coulomb interactions are  $U_{BB} = 15\gamma$  and  $U_{AA} = U_{CC}$ . Parameters not mentioned remain the same as in previous plots.

here the minimum current is still greater than 60% of the maximum. We attribute this to the fact that the Aharonov-Bohm interference is a single-particle effect, at least in the manner we have included it. The two paths available around the TQD allow electrons to accumulate a phase difference with their own wavefunction, but there are still potentially two other electrons with which to form a three-particle wavefunction, diminishing the importance of the Aharonov-Bohm effect.

Interestingly, we note that the current profiles of both configurations are identical for triple-occupancy. In contrast, the Pearson coefficient, shown in Figs.(6c)-(6d), displays quantitatively different behavior between the two configurations; this is a potential method of experimental identification between the two TQD configurations. Aharonov-Bohm interference clearly affects the correlation behavior, as  $p$  displays periodic oscillations in  $\phi$ . Ultimately, this is a very interesting research avenue, as the potential for tuning correlations with magnetic flux could lead to novel information processing methods. At this point, however, the Pearson coefficient is quite small:  $|p| \leq 0.1$ . In the reverse configuration, we might expect larger correlations; two dots are connected to the drain and so coherent electrons may be detected simultaneously. The Pearson coefficient does actually increase in magnitude for the reverse configuration, but it is still small:  $|p| < 0.2$ . To analyze further, we turn to  $W(\tau_1, \tau_2)$ , displayed in Fig.(7), which provides correlation information for each pair of successive waiting

	$\tau_1 = 4.3\langle\tau\rangle$	$\tau_1 = 0.08\langle\tau\rangle$
$P_0$	0.001	0.27
$\langle a_A^\dagger a_A \rangle$	0.97	0.57
$\langle a_B^\dagger a_B \rangle$	0	0
$\langle a_C^\dagger a_C \rangle$	0.97	0.19

TABLE I: Table of occupation probabilities for two different initial waiting times  $\tau_1$  and  $\tau_2$ .

times.

There are multiple points of interest in Fig.(7); however, we will discuss just a few. In the left column, which is computed for the configuration in Fig.(1a), at  $\phi = \pi$  and  $\phi = \frac{\pi}{2}$ , respectively, there are regimes of both positive and negative correlations. The probability of observing a long waiting time followed by a short waiting time is comparably more than the uncorrelated case, and likewise the probability of observing a short waiting time followed by a long one is also increased compared to the uncorrelated case. These differences are much greater than what the Pearson correlation coefficient, being an average measure, captures.

Table I shows that this correlation behavior can be understood via occupation probabilities. When  $\tau_1 = 0.08\langle\tau\rangle$ , for example, the probability that the second jump leaves the dot empty, denoted by  $P_0$ , is 0.27, so it is likely that before another electron can tunnel out to the drain an electron will first have to tunnel in from the

source, increasing the probability that the second waiting time will be longer than average. When  $\tau_1 = 4.3\langle\tau\rangle$ , on the other hand, dots  $A$  and  $C$  are almost always occupied, so the strong inter-dot couplings can bring an electron to the  $B$  dot quickly.

These features are not unique to Fig.(7b), however, and in fact all plots in Fig.(7) display similar behavior. In fact, because we have chosen  $\phi = \pi$  in the top row, the two configurations display similar behavior. Both have a highly structured repeating patterned, which is due to coherent oscillations in  $w(\tau_1, \tau_2)$ . Aharonov-Bohm interference, however, breaks this structure and ‘washes out’ the pattern, albeit keeping the magnitude of correlations the same; this can be seen in the bottom row where  $\phi = \frac{\pi}{2}$ .

### C. Spin-dependent double-occupancy

For spin-dependent double-occupancy, each dot may be occupied by one or two excess electrons, but the TQD as a whole has a maximum occupancy of two. In this regime, Polt et al. [40] found that for certain parameters a two-particle dark state forms when the inter-dot repulsion between  $A$  and  $C$  is equal to the intra-dot repulsion within  $A$ :  $\delta U = U_{AA} - U_{AC} = 0$ . Their configuration did not allow tunneling between dot  $A$  and  $C$ , however, and we demonstrate in Fig.(8a) that a dark state exists for the same parameters even when dots  $A$  and  $C$  are coherently coupled. The dark state can be tuned by  $\delta U$  and, now that tunneling between  $A$  and  $C$  is allowed, the magnetic flux penetrating the ring.

As expected, the correlation between successive waiting times reaches peak magnitude when coherent population blocking is strongest:  $\phi = n\pi$  for  $\delta U/|t| = 0.1$  in Fig.(8a). The Pearson coefficient, however, is still underwhelming,  $|p| < 0.1$ , which indicates that a high level of destructive interference does not necessarily produce strong correlations. It is also apparent from Fig.(8b) that significant correlations exist even without the formation of a dark state; the  $|p|$  maximum occurs when  $\langle I \rangle$  is also a maximum. In this configuration, furthermore, we see the particularly interesting result that correlations can be tuned from positive to negative with  $\phi$ , as long as  $\delta U/|t| \geq 5$ .

To go beyond just the Pearson coefficient, we again turn to  $W(\tau_1, \tau_2)$  in Fig.(9). Unlike the triple-occupancy regime, double-occupancy  $W(\tau_1, \tau_2)$  shows little repeating structure and is not necessarily symmetric under interchange of  $\tau_1 \leftrightarrow \tau_2$ . In Fig.(9a), for example, there is a band of negatively correlated times at small  $\tau_2$ . That is, if the first waiting time  $\tau_1$  is less than  $0.5\langle\tau\rangle$ , it is highly unlikely the waiting time until the next jump  $\tau_2$  will be extremely short. We can attribute this behavior to there being three quantum jumps involved but only two electrons allowed in the TQD; if  $\tau_1 < 0.5\langle\tau\rangle$ , it is likely that the TQD fully empties before the third quantum jump. One might expect, conversely, that observing  $\tau_1 > \langle\tau\rangle$  would then be positively correlated with  $\tau_2 < \langle\tau\rangle$ . How-

ever, in this configuration and for  $\phi = \pi$ ,  $W(\tau_1, \tau_2)$  decays for  $\tau_1, \tau_2 > 0.5\langle\tau\rangle$ , hence why we have plotted for  $\tau_1, \tau_2 < 0.5\langle\tau\rangle$  only.

Fig.(9c) shows that when one imposes a phase difference via  $\phi = \frac{\pi}{2}$ , then all structure from  $W(\tau_1, \tau_2)$  disappears but that correlations become stronger and also last longer. For  $\tau_2 < 0.25\langle\tau\rangle$  and at  $\tau_1 \approx 1.3\langle\tau\rangle$  and  $\tau_1 \approx 1.75\langle\tau\rangle$ , we also see strong positive and negative correlations neighboring each other with only a small uncorrelated area inbetween. This is strange behavior compared to other plots of  $W(\tau_1, \tau_2)$ , in which there are usually large zones of uncorrelated  $\tau_1, \tau_2$  between areas of strong positive and negative correlations.

Indeed, one can observe this in Fig.(9b) for the opposite configuration. An initial waiting time much longer than the average, for example  $\tau_1 = 3\langle\tau\rangle$ , is positively correlated with a short second waiting time  $\tau_2 < 0.5\langle\tau\rangle$ , as there has been time for the TQD to fill. As expected, the opposite scenario of short  $\tau_1$  and long  $\tau_2$  is also positively correlated, although we note that again it is not symmetric. Pairs of waiting times that are both shorter or longer than average are correspondingly negatively correlated. Applying a phase difference of  $\phi = \frac{\pi}{2}$  now only serves to extend the regions of correlations, but does not change the overall structure. Now that two dots are coupled to the drain, the system can behave in the multiple-reset nature, which results in the more standard  $W(\tau_1, \tau_2)$ .

## VI. CONCLUSION

The TQD is a rich experimental and theoretical system displaying coherent phenomena, such as Aharonov-Bohm oscillations and coherent population blocking. Although it has previously been subjected to fluctuation analysis via FCS in the long-time limit, there is little literature exploring fluctuating-time statistics in this regime. In this paper, therefore, we applied the WTD to a triangular TQD under two geometries in three regimes: spin-independent single- and triple-occupancy and spin-dependent double-occupancy:

- In the single-occupancy regime, where only one excess electron is allowed in the TQD, we found that coherent oscillations present in the WTD itself, which correlate to occupation probabilities of dots coupled to the drain and depend on the orientation of the TQD.
- From the time-dependent occupation probabilities, we are able to see the effect of tuning the Aharonov-Bohm interference on electron tunneling direction in the single-occupancy regime. In the regime of strong inter-dot coupling, furthermore, there exist interesting global and local temporal oscillations for which the underlying dynamics are currently an open question.
- Although it is well known that a dark state exists in the single-occupancy regime, we showed that

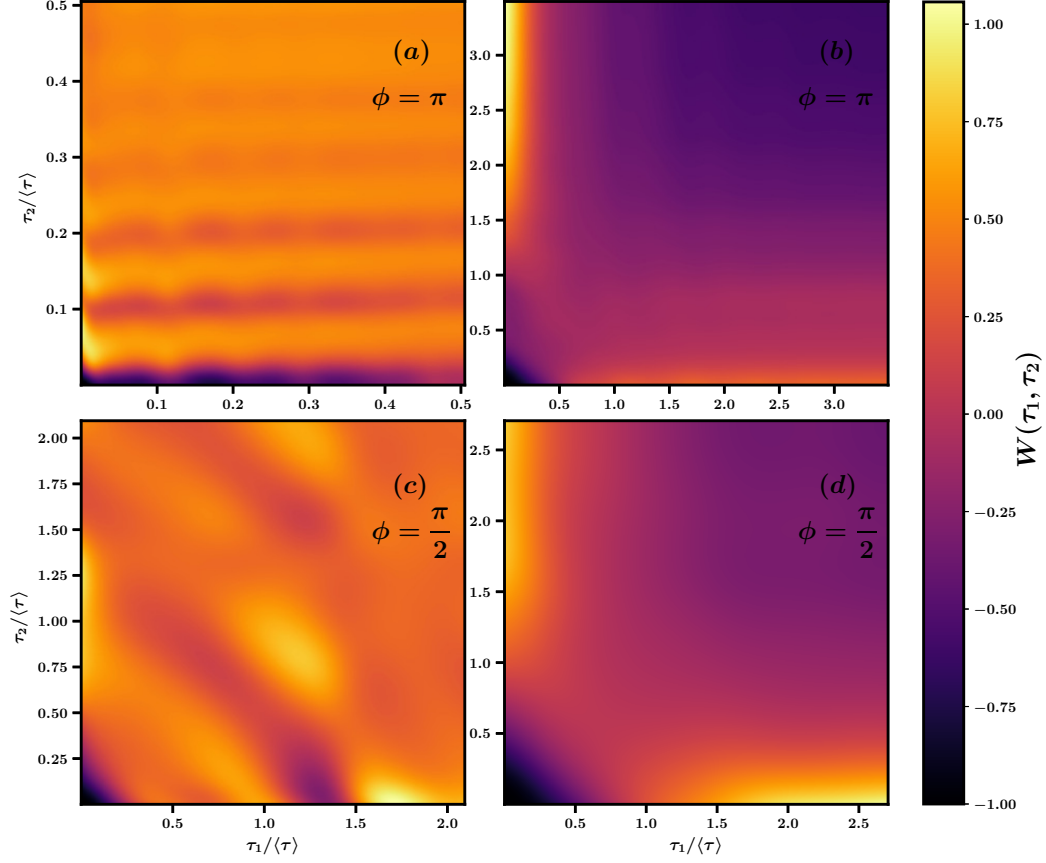


FIG. 9:  $W(\tau_1, \tau_2)$  with the same ordering of configurations and magnetic flux as in Fig.(7). We use the same parameters as in Fig.(8), choosing  $\delta U/|t| = 1$  and  $\delta U/|t| = 5$  for the left and right columns, respectively.

triple-occupancy largely removes coherent population blocking.

- In this regime, additionally, the Pearson correlation coefficient is non-zero, although still quite small, and it displays similar periodic, albeit more complicated, behavior to the stationary current. The quantity  $W(\tau_1, \tau_2)$ , shows that, in the triple-occupancy regime, correlations have a highly repeating structure when  $\phi = \pi$ , but that this structure is largely destroyed by applying  $\phi = \frac{\pi}{2}$ .
- The double-occupancy regime, by contrast, displays relatively unstructured correlation behavior. There are also more significant differences between the two TQD configurations in this regime, most likely due to the fact that each dot in the TQD may now be doubly occupied. Overall, the average Pearson correlation coefficient is stronger in this regime too.

- Finally, we also demonstrated that the dark state found by Poltl et al. [40, 41] and Busl et al. [42] extends to a TQD where all dots are coupled, and that, like the single-occupancy regime, this dark state can be tuned via a penetrating magnetic flux.

#### Appendix A: Master equation derivation

First, we condense the bath operators into

$$\begin{aligned}
 d^\dagger &= \sum_{\alpha} d_{\alpha}^{\dagger} & \text{and} & & d &= \sum_{\alpha} d_{\alpha} \\
 &= \sum_{\alpha} \sum_{\mathbf{k}_{\alpha}} t_{\mathbf{k}_{\alpha}} a_{\mathbf{k}_{\alpha}}^{\dagger} & & & &= \sum_{\alpha} \sum_{\mathbf{k}_{\alpha}} t_{\mathbf{k}_{\alpha}} a_{\mathbf{k}_{\alpha}}. \quad (\text{A1})
 \end{aligned}$$

Since we are measuring in one electrode only, we will separate the source and drain parts of the master equation, writing explicitly here only the drain contribution after including the explicit form of  $V_I(t)$  in Eq.(13):

$$\dot{\rho}_I^{(n)}(t) = - \int_0^t d\tau \sum_{qq'} \sum_{n'} \text{Tr}_{B^{(n)}} \left[ \mathcal{M}_I(t) a_{q,I}^\dagger(t) d_{D,I}(t) - \mathcal{M}_I^\dagger(t) a_{q',I}(t) d_{D,I}^\dagger(t), \right. \\ \left. \left[ \mathcal{M}_I(t-\tau) a_{q',I}^\dagger(t-\tau) d_{D,I}(t-\tau) - \mathcal{M}_I^\dagger(t-\tau) a_{q,I}(t-\tau) d_{D,I}^\dagger(t-\tau), \rho_I^{(n')}(t-\tau) \rho_S \rho_D |n'\rangle \langle n'| \right] \right]. \quad (\text{A2})$$

We can consider the source and drain contributions to the master equations additively because under the trace any terms containing operators from different electrodes will disappear. In Eq.(A2), we have also applied the weak coupling ansatz from Eq.(14).

While the nanostructure and bath operators have their usual form in the interaction picture, it is necessary to discuss the measurement operators,

$$\mathcal{M}_I(t) = \sum_n e^{i(\varepsilon_{n-1} - \varepsilon_n)t} |n-1\rangle \langle n| \quad (\text{A3})$$

$$\mathcal{M}_I^\dagger(t) = \sum_n e^{i(\varepsilon_n - \varepsilon_{n-1})t} |n\rangle \langle n-1|, \quad (\text{A4})$$

because at this point we assume that the detector expends a negligible amount of energy in recording each tunneling, so that  $|\varepsilon_{n-1} - \varepsilon_n|t \approx 0$ , resulting in  $\mathcal{M}_I(t) = \mathcal{M}$  and  $\mathcal{M}_I^\dagger(t) = \mathcal{M}^\dagger$ .

Expanding now the commutators from Eq.(A2), excluding terms with  $d_{D,I} d_{D,I}$  or  $d_{D,I}^\dagger d_{D,I}^\dagger$  as they disappear under the trace, and collecting all measurement operators and detector states, the master equation reads

$$\dot{\rho}_I^{(n')}(t) = \int_0^t d\tau \sum_{qq'} \sum_{n'} \text{Tr}_B \left( |n\rangle \langle n| \mathcal{M} \mathcal{M}^\dagger |n'\rangle \langle n'| a_{q,I}^\dagger(t) d_I(t) a_{q',I}(t-\tau) d_I^\dagger(t-\tau) \rho_I^{(n')}(t) \rho_S \rho_D \right. \\ + |n\rangle \langle n| \mathcal{M}^\dagger \mathcal{M} |n'\rangle \langle n'| a_{q,I}(t) d_I^\dagger(t) a_{q',I}^\dagger(t-\tau) d_I(t-\tau) \rho_I^{(n')}(t-\tau) \rho_S \rho_D \\ - |n\rangle \langle n| \mathcal{M} |n'\rangle \langle n'| \mathcal{M}^\dagger a_{q,I}^\dagger(t) d_I(t) \rho_I^{(n')}(t-\tau) \rho_S \rho_D a_{q',I}(t-\tau) d_I^\dagger(t-\tau) \\ - |n\rangle \langle n| \mathcal{M}^\dagger |n'\rangle \langle n'| \mathcal{M} a_{q,I}(t) d_I^\dagger(t) \rho_I^{(n')}(t-\tau) \rho_S \rho_D a_{q',I}^\dagger(t-\tau) d_I(t-\tau) \\ - |n\rangle \langle n| \mathcal{M} |n'\rangle \langle n'| \mathcal{M}^\dagger a_{q',I}^\dagger(t-\tau) d_I(t-\tau) \rho_I^{(n')}(t-\tau) \rho_S \rho_D a_{q,I}(t) d_I^\dagger(t) \\ - |n\rangle \langle n| \mathcal{M}^\dagger |n'\rangle \langle n'| \mathcal{M} a_{q',I}(t-\tau) d_I^\dagger(t-\tau) \rho_I^{(n')}(t-\tau) \rho_S \rho_D a_{q,I}^\dagger(t) d_I(t) \\ + |n\rangle \langle n| n' \rangle \langle n'| \mathcal{M} \mathcal{M}^\dagger \rho_I^{(n')}(t-\tau) \rho_S \rho_D a_{q',I}^\dagger(t-\tau) d_I(t-\tau) a_{q,I}(t) d_I^\dagger(t) \\ \left. + |n\rangle \langle n| n' \rangle \langle n'| \mathcal{M} \mathcal{M}^\dagger \rho_I^{(n')}(t-\tau) \rho_S \rho_D a_{q',I}(t-\tau) d_I^\dagger(t-\tau) a_{q,I}^\dagger(t) d_I(t) \right). \quad (\text{A5})$$

This removes the summation over  $n'$  and transforms

the master equation to

$$\dot{\rho}_I^{(n)}(t) = \int_0^t d\tau \sum_{qq'} \text{Tr}_B \left\{ |n\rangle \langle n| \left( a_{q,I}^\dagger(t) d_I(t) a_{q',I}(t-\tau) d_I^\dagger(t-\tau) \rho_I^{(n)}(t-\tau) \rho_S \rho_D \right. \right. \\ + a_{q,I}(t) d_I^\dagger(t) a_{q',I}^\dagger(t-\tau) d_I(t-\tau) \rho_I^{(n)}(t-\tau) \rho_S \rho_D - a_{q,I}^\dagger(t) d_I(t) \rho_I^{(n)}(t-\tau) \rho_S \rho_D a_{q',I}(t-\tau) d_I^\dagger(t-\tau) \\ - a_{q,I}(t) d_I^\dagger(t) \rho_I^{(n)}(t-\tau) \rho_S \rho_D a_{q',I}^\dagger(t-\tau) d_I(t-\tau) - a_{q',I}^\dagger(t-\tau) d_I(t-\tau) \rho_I^{(n)}(t-\tau) \rho_S \rho_D a_{q,I}(t) d_I^\dagger(t) \\ - a_{q',I}(t-\tau) d_I^\dagger(t-\tau) \rho_I^{(n)}(t-\tau) \rho_S \rho_D a_{q,I}^\dagger(t) d_I(t) + \rho_I^{(n)}(t-\tau) \rho_S \rho_D a_{q',I}^\dagger(t-\tau) d_I(t-\tau) a_{q,I}(t) d_I^\dagger(t) \\ \left. \left. + \rho_I^{(n)}(t-\tau) \rho_S \rho_D a_{q',I}(t-\tau) d_I^\dagger(t-\tau) a_{q,I}^\dagger(t) d_I(t) \right) \right\}. \quad (\text{A6})$$

The trace over the detector space is removed by the pro-

jector  $|n\rangle \langle n|$ , so that  $\text{Tr}_B [\dots]$  yields the standard bath-

correlation functions:

$$\begin{aligned} G_\alpha^>(\tau) &= \text{Tr}_B \left( \rho_B d_{\alpha,I}(t) d_I^\dagger(t-\tau) \right) \\ G_\alpha^<(\tau) &= \text{Tr}_B \left( \rho_B d_I^\dagger(t) d_{\alpha,I}(t-\tau) \right). \end{aligned} \quad (\text{A7})$$

Finally, we apply Markovianity after returning from the interaction picture, so that  $\rho(t-\tau) \approx \rho(t)$  and

$$\begin{aligned} \dot{\rho}^{(n)}(t) &= \left[ H_Q, \rho^{(n)}(t) \right] - i \sum_{qq'} \int_0^\infty d\tau \left( \sum_\alpha \left[ G_\alpha^>(\tau) a_q^\dagger e^{-iH_Q\tau} a_{q'} e^{iH_Q\tau} \rho^{(n)}(t) + G_\alpha^<(\tau) a_{q'} e^{-iH_Q\tau} a_q^\dagger e^{iH_Q\tau} \rho^{(n)}(t) \right] \right. \\ &\quad - \left[ G_S^>(\tau) e^{-iH_Q\tau} a_{q'} e^{iH_Q\tau} \rho^{(n)}(t) a_q^\dagger + G_S^<(\tau) e^{-iH_Q\tau} a_q^\dagger e^{iH_Q\tau} \rho^{(n)}(t) a_q + G_D^>(\tau) e^{-iH_Q\tau} a_{q'} e^{iH_Q\tau} \rho^{(n-1)}(t) a_q^\dagger \right. \\ &\quad \left. \left. + G_D^<(\tau) e^{-iH_Q\tau} a_q^\dagger e^{iH_Q\tau} \rho^{(n+1)}(t) a_q \right] + \text{h.c.} \right). \end{aligned} \quad (\text{A8})$$

Performing the integral and defining lesser,  $\Sigma_\alpha^<(\omega_{mn})$ , and greater,  $\Sigma_\alpha^>(\omega_{mn})$  self-energies as

$$\begin{aligned} \Sigma_\alpha^<(\omega_{mn}) &= i \int_0^\infty d\tau e^{-i\omega_{nm}\tau} G_\alpha^<(-\tau) \\ \Sigma_\alpha^>(\omega_{mn}) &= -i \int_0^\infty d\tau e^{-i\omega_{nm}\tau} G_\alpha^>(-\tau), \end{aligned} \quad (\text{A9})$$

we get the master equation in Eq.(15).

### Appendix B: TQD triple-occupancy

In defining the individual equations of motion, it is expedient to define coefficients for the overlap between the

transformed single- and two-particle energy eigenstates as

$$D_{1i,1j} = \sum_{\nu=\{A,C\}} \langle 0|a_\nu|1i\rangle \langle 1j|a_\nu^\dagger|0\rangle \quad (\text{B1})$$

$$G_{2r,2s} = \sum_{\nu=\{A,C\}} \langle 3|a_\nu^\dagger|2r\rangle \langle 2s|a_\nu|3\rangle \quad (\text{B2})$$

$$E_{2r,2s,1i,1j} = \sum_{\nu=\{A,C\}} \langle 1i|a_\nu|2r\rangle \langle 2s|a_\nu^\dagger|1j\rangle \quad (\text{B3})$$

$$F_{2r,2s,1i,1j} = \langle 1i|a_B|2r\rangle \langle 2s|a_B^\dagger|1j\rangle. \quad (\text{B4})$$

The master equations for each element are

$$\begin{aligned} \dot{\rho}_{0,0} &= -i\rho_{0,0} \left( \sum_{1i} D_{1i,1i} (\Sigma_S^<(\omega_{1i,0}) - \Sigma_S^<(\omega_{1i,0})^*) + |c_{1i,B}|^2 (\Sigma_D^<(\omega_{1i,0}) - \Sigma_D^<(\omega_{1i,0})^*) \right. \\ &\quad \left. - i \sum_{1j} \sum_{1i} \rho_{1i,1j} [D_{1i,1j} (\Sigma_S^>(\omega_{1j,0})^* - \Sigma_S^>(\omega_{1i,0})) + e^{i\chi} c_{1i,B} c_{1j,B}^* (\Sigma_D^>(\omega_{1j,0})^* - \Sigma_D^>(\omega_{1i,0}))] \right), \end{aligned} \quad (\text{B5})$$

$$\begin{aligned} \dot{\rho}_{1i,1j} &= -i\omega_{1i,1j} - i\rho_{0,0} [D_{1j,1i} (\Sigma_S^<(\omega_{1j,0}) - \Sigma_S^<(\omega_{1i,0})^*) + e^{-i\chi} c_{1j,B} c_{1i,B}^* (\Sigma_D^<(\omega_{1j,0}) - \Sigma_D^<(\omega_{1i,0})^*)] \\ &\quad - i \left[ \sum_{1k} \left( \rho_{1k,1j} [D_{1k,1i} \Sigma_S^>(\omega_{1k,0}) + c_{1k,B} c_{1i,B}^* \Sigma_D^>(\omega_{1k,0}) + \sum_{2r} (E_{2r,2r,1i,1k} \Sigma_S^<(\omega_{2r,1k})^* \right. \right. \\ &\quad \left. \left. + F_{2r,2r,1i,1k} \Sigma_D^<(\omega_{2r,1k})^*) \right] - \rho_{1i,1k} [D_{1j,1k} \Sigma_S^>(\omega_{1k,0})^* + c_{1j,B} c_{1k,B}^* \Sigma_D^>(\omega_{1k,0})^* \right. \\ &\quad \left. + \sum_{2r} (E_{2r,2r,1k,1j} \Sigma_S^<(\omega_{2r,1k}) + F_{2r,2r,1k,1j} \Sigma_D^<(\omega_{2r,1k})) \right] + \sum_{2s} \sum_{2r} \rho_{2r,2s} [E_{2r,2s,1i,1j} (\Sigma_S^>(\omega_{2s,1j})^* \\ &\quad \left. - \Sigma_S^>(\omega_{2r,1i})) + e^{i\chi} F_{2r,2s,1i,1j} (\Sigma_D^>(\omega_{2s,1j})^* - \Sigma_D^>(\omega_{2r,1i})) \right], \end{aligned} \quad (\text{B6})$$

$$\begin{aligned}
\dot{\rho}_{2r,2s} = & -i\omega_{2r,2s} - i\rho_{3,3} \left[ G_{2s,2r} (\Sigma_S^>(\omega_{3,2s})^* - \Sigma_S^>(\omega_{3,2r})) + e^{i\chi} c_{2r,AC} c_{2s,AC}^* (\Sigma_D^>(\omega_{3,2s})^* - \Sigma_D^>(\omega_{3,2r})) \right] \\
& - i \left[ \sum_{2t} \left( \rho_{2t,2s} \left[ G_{2t,2r} \Sigma_S^<(\omega_{3,2t})^* + c_{2t,AC} c_{2r,AC}^* \Sigma_D^<(\omega_{3,2t})^* + \sum_{1i} (E_{2t,2r,1i,1i} \Sigma_S^>(\omega_{2t,1i}) \right. \right. \right. \\
& \left. \left. \left. + F_{2t,2r,1i,1i} \Sigma_D^>(\omega_{2t,1i}) \right) \right] - \rho_{2r,2t} \left[ G_{2s,2t} \Sigma_S^<(\omega_{3,2t}) + c_{2s,AC} c_{2t,AC}^* \Sigma_D^<(\omega_{3,2t}) \right. \right. \\
& \left. \left. + \sum_{1i} (E_{2s,2t,1i,1i} \Sigma_S^>(\omega_{2t,1i})^* + F_{2s,2t,1i,1i} \Sigma_D^>(\omega_{2t,1i})^*) \right] \right) + \sum_{1j} \sum_{1i} \rho_{1i,1j} \left[ E_{2s,2r,1j,1i} (\Sigma_S^<(\omega_{2s,1j}) \right. \\
& \left. \left. - \Sigma_S^<(\omega_{2r,1i})^*) + e^{-i\chi} F_{2s,2r,1j,1i} (\Sigma_D^<(\omega_{2s,1j}) - \Sigma_D^<(\omega_{2r,1i})^*) \right] \right], \quad \text{and} \quad (B7)
\end{aligned}$$

$$\begin{aligned}
\dot{\rho}_{3,3} = & -i\rho_{3,3} \left( \sum_{2r} G_{2r,2r} (\Sigma_S^>(\omega_{3,2r}) - \Sigma_S^>(\omega_{3,2r})^*) + |c_{2r,AC}|^2 (\Sigma_D^>(\omega_{3,2r}) - \Sigma_D^>(\omega_{3,2r})^*) \right) \\
& - i \sum_{2s} \sum_{2r} \rho_{2r,2s} \left[ G_{2r,2s} (\Sigma_S^<(\omega_{3,2s}) - \Sigma_S^<(\omega_{3,2r})^*) + e^{-i\chi} c_{1i,B} c_{1j,B}^* (\Sigma_D^<(\omega_{3,2s}) - \Sigma_D^<(\omega_{3,2r})^*) \right]. \quad (B8)
\end{aligned}$$

---

For the configuration in Fig.(1b),  $\Sigma_S(\omega) \leftrightarrow \Sigma_D(\omega)$ .

---

- [1] G. Engelhardt and J. Cao, *Phys. Rev. B* **99**, 075436 (2019).
- [2] X. Guo, A. Whalley, J. E. Klare, L. Huang, S. O'Brien, M. Steigerwald, and C. Nuckolls, *Nano Lett.* **7**, 1119 (2007).
- [3] J. Cuevas and E. Scheer, *Molecular Electronics: An Introduction to Theory and Experiment* (World Scientific, Singapore, 2010).
- [4] D. Xiang, X. Wang, C. Jia, T. Lee, and X. Guo, *Chem. Rev.* **116**, 4318 (2016).
- [5] J. Koch, F. von Oppen, and A. V. Andreev, *Phys. Rev. B* **74**, 205438 (2006).
- [6] C. Schinabeck, A. Erpenbeck, R. Härtle, and M. Thoss, *Phys. Rev. B* **94**, 201407 (2016).
- [7] C. Schinabeck, R. Härtle, and M. Thoss, *Phys. Rev. B* **97**, 235429 (2018).
- [8] T. K. Ng and P. A. Lee, *Phys. Rev. Lett.* **61**, 1768 (1988).
- [9] L. Gaudreau, S. A. Studenikin, A. S. Sachrajda, P. Zawadzki, A. Kam, J. Lapointe, M. Korkusinski, and P. Hawrylak, *Phys. Rev. Lett.* **97**, 036807 (2006).
- [10] M. Korkusinski, I. P. Gimenez, P. Hawrylak, L. Gaudreau, S. A. Studenikin, and A. S. Sachrajda, *Phys. Rev. B* **75**, 115301 (2007).
- [11] L. Gaudreau, A. S. Sachrajda, S. Studenikin, P. Zawadzki, A. Kam, and J. Lapointe, *AIP Conf. Proc.* **893**, 857 (2007).
- [12] L. Gaudreau, A. S. Sachrajda, S. Studenikin, A. Kam, F. Delgado, Y. P. Shim, M. Korkusinski, and P. Hawrylak, *Phys. Rev. B* **80**, 075415 (2009).
- [13] W. G. van der Wiel, S. De Franceschi, J. M. Elzerman, T. Fujisawa, S. Tarucha, and L. P. Kouwenhoven, *Rev. Mod. Phys.* **75**, 1 (2002).
- [14] D. Schröer, A. D. Greentree, L. Gaudreau, K. Eberl, L. C. L. Hollenberg, J. P. Kotthaus, and S. Ludwig, *Phys. Rev. B* **76**, 075306 (2007).
- [15] M. C. Rogge and R. J. Haug, *Phys. Rev. B* **77**, 193306 (2008).
- [16] S. Amaha, T. Hatano, T. Kubo, Y. Tokura, D. G. Austing, and S. Tarucha, *Phys. E* **40**, 1322 (2008).
- [17] S. Amaha, W. Izumida, T. Hatano, S. Teraoka, S. Tarucha, J. A. Gupta, and D. G. Austing, *Phys. Rev. Lett.* **110**, 016803 (2013).
- [18] M. Pioro-Ladrière, T. Obata, Y. Tokura, Y.-S. Shin, T. Kubo, K. Yoshida, T. Taniyama, and S. Tarucha, *Nat. Phys.* **4**, 776 (2008).
- [19] T. Takakura, M. Pioro-Ladrière, T. Obata, Y.-S. Shin, R. Brunner, K. Yoshida, T. Taniyama, and S. Tarucha, *Appl. Phys. Lett.* **97**, 212104 (2010).
- [20] M. Russ and G. Burkard, *J. Phys. Condens. Matter* **29**, 393001 (2017).
- [21] E. A. Laird, J. M. Taylor, D. P. DiVincenzo, C. M. Marcus, M. P. Hanson, and A. C. Gossard, *Phys. Rev. B* **82**, 075403 (2010).
- [22] L. Gaudreau, G. Granger, A. Kam, G. C. Aers, S. A. Studenikin, P. Zawadzki, M. Pioro-Ladrière, Z. R. Wasilewski, and A. S. Sachrajda, *Nat. Phys.* **8**, 54 (2012).
- [23] R. Sánchez, G. Granger, L. Gaudreau, A. Kam, M. Pioro-Ladrière, S. A. Studenikin, P. Zawadzki, A. S. Sachrajda, and G. Platero, *Phys. Rev. Lett.* **112**, 176803 (2014).
- [24] J. Luczak and B. R. Buřka, *Phys. Rev. B* **90**, 165427 (2014).
- [25] J. Luczak and B. R. Buřka, *Quantum Inf. Process.* **16**, 10 (2016).
- [26] A. K. Mitchell, T. F. Jarrold, and D. E. Logan, *Phys. Rev. B* **79**, 085124 (2009).
- [27] M. Seo, H. K. Choi, S.-Y. Lee, N. Kim, Y. Chung, H.-S. Sim, V. Umansky, and D. Mahalu, *Phys. Rev. Lett.* **110**, 046803 (2013).
- [28] D. S. Saraga and D. Loss, *Phys. Rev. Lett.* **90**, 166803 (2003).

- [29] Z.-t. Jiang, Q.-f. Sun, and Y. Wang, *Phys. Rev. B* **72**, 045332 (2005).
- [30] R. Žitko, J. Bonča, A. Ramšak, and T. Rejec, *Phys. Rev. B* **73**, 153307 (2006).
- [31] T. Numata, Y. Nisikawa, A. Oguri, and A. C. Hewson, *Phys. Rev. B* **80**, 155330 (2009).
- [32] Y. Cheng, Y. Wang, J. Wei, Z. Zhu, and Y. Yan, *Phys. Rev. B* **95**, 155417 (2017).
- [33] R. López, T. Rejec, J. Martinek, and R. Žitko, *Phys. Rev. B* **87**, 035135 (2013).
- [34] E. Vernek, C. A. Büsser, G. B. Martins, E. V. Anda, N. Sandler, and S. E. Ulloa, *Phys. Rev. B* **80**, 035119 (2009).
- [35] A. Oguri, S. Amaha, Y. Nishikawa, T. Numata, M. Shimamoto, A. C. Hewson, and S. Tarucha, *Phys. Rev. B* **83**, 205304 (2011).
- [36] T. Kuzmenko, K. Kikoin, and Y. Avishai, *Phys. Rev. Lett.* **96**, 046601 (2006).
- [37] C. W. Groth, B. Michaelis, and C. W. J. Beenakker, *Phys. Rev. B* **74**, 125315 (2006).
- [38] B. Michaelis, C. Emary, and C. W. J. Beenakker, *EPL* **73**, 677 (2006).
- [39] C. Emary, *Phys. Rev. B* **76**, 245319 (2007).
- [40] C. Pörtl, C. Emary, and T. Brandes, *Phys. Rev. B* **80**, 115313 (2009).
- [41] C. Pörtl, C. Emary, and T. Brandes, *Phys. Rev. B* **87**, 045416 (2013).
- [42] M. Busl, R. Sánchez, and G. Platero, *Phys. Rev. B* **81**, 121306 (2010).
- [43] T. Kostyrko and B. R. Bulka, *Phys. Rev. B* **79**, 075310 (2009).
- [44] I. Weymann, B. R. Bulka, and J. Barnaś, *Phys. Rev. B* **83**, 195302 (2011).
- [45] A. Noiri, T. Takakura, T. Obata, T. Otsuka, T. Nakajima, J. Yoneda, and S. Tarucha, *Phys. Rev. B* **96**, 155414 (2017).
- [46] M. Niklas, A. Trottmann, A. Donarini, and M. Grifoni, *Phys. Rev. B* **95**, 115133 (2017).
- [47] B. R. Bulka, T. Kostyrko, and J. Luczak, *Phys. Rev. B* **83**, 035301 (2011).
- [48] T. Brandes, *Ann. Phys. (Berlin)* **17**, 477 (2008).
- [49] M. Srinivas and E. Davies, *Opt. Acta* **28**, 981 (2010).
- [50] K. H. Thomas and C. Flindt, *Phys. Rev. B* **87**, 121405 (2013).
- [51] D. S. Kosov, *J. Chem. Phys.* **147**, 104109 (2017).
- [52] D. Dasenbrook, P. P. Hofer, and C. Flindt, *Phys. Rev. B* **91**, 195420 (2015).
- [53] M. Albert, C. Flindt, and M. Büttiker, *Phys. Rev. Lett.* **107**, 086805 (2011).
- [54] M. Albert, G. Haack, C. Flindt, and M. Büttiker, *Phys. Rev. Lett.* **108**, 186806 (2012).
- [55] M. Albert, D. Chevallier, and P. Devillard, *Phys. E* **76**, 209 (2016).
- [56] M. Albert and P. Devillard, *Phys. Rev. B* **90**, 035431 (2014).
- [57] D. Chevallier, M. Albert, and P. Devillard, *EPL* **116**, 27005 (2016).
- [58] G. Haack, M. Albert, and C. Flindt, *Phys. Rev. B* **90**, 205429 (2014).
- [59] K. Ptaszyński, *Phys. Rev. B* **96**, 035409 (2017).
- [60] K. Ptaszyński, *Phys. Rev. B* **95**, 045306 (2017).
- [61] K. Ptaszyński, *Phys. Rev. E* **97**, 012127 (2018).
- [62] S. Welack, S. Mukamel, and Y. J. Yan, *EPL* **85**, 57008 (2009).
- [63] X.-Q. Li, P. Cui, and Y. Yan, *Phys. Rev. Lett.* **94**, 066803 (2005).
- [64] X.-Q. Li, J. Luo, Y.-G. Yang, P. Cui, and Y.-J. Yan, *Phys. Rev. B* **71**, 205304 (2005).
- [65] H. Breuer, F. Petruccione, and S. Petruccione, *The Theory of Open Quantum Systems* (Oxford University Press, London, 2002).
- [66] M. Abramowitz, *Handbook of Mathematical Functions, With Formulas, Graphs, and Mathematical Tables*, (Dover Publications, Inc., USA, 1974).
- [67] D. A. Bagrets and Y. V. Nazarov, *Phys. Rev. B* **67**, 085316 (2003).
- [68] Y. V. Nazarov, [arXiv.org](https://arxiv.org/abs/1909.00001) (1999).
- [69] Y. Aharonov and D. Bohm, *Phys. Rev.* **115**, 485 (1959).
- [70] A. A. Budini, *Phys. Rev. E* **84**, 011141 (2011).
- [71] S. L. Rudge and D. S. Kosov, *J. Chem. Phys.* **144**, 124105 (2016).
- [72] S. L. Rudge and D. S. Kosov, *Phys. Rev. E* **94**, 042134 (2016).
- [73] S. L. Rudge and D. S. Kosov, 245402 (2018).
- [74] S. L. Rudge and D. S. Kosov, *Phys. Rev. B* **99**, 115426 (2019).
- [75] S. L. Rudge and D. S. Kosov, *Phys. Rev. B* **100**, 235430 (2019).